A. Gorgeri, R. Vescovini, L. Dozio
Sublaminate Variable Kinematics Shell Models for Functionally Graded Sandwich Panels: Bending and Free Vibration Response
Mechanics of Advanced Materials and Structures, In press - Published online 16/04/2020
doi:10.1080/15376494.2020.1749738

Sublaminate variable kinematics shell models for functionally graded sandwich panels: Bending and free vibration response

A. Gorgeri, R. Vescovini*and L. Dozio

Dipartimento di Scienze e Tecnologie Aerospaziali, Politecnico di Milano

Via La Masa 34, 20156 Milano, Italy

Abstract

An advanced kinematic formulation is applied to multilayered cylindrical sandwich panels with continuously graded layers. Free vibration and bending problems are considered. The mean mechanical properties of the composite material are estimated by means of the extended rule of mixture or the Eshelby-Mori-Tanaka method. The displacement field is postulated by means of variable-kinematics sublaminate models, therefore the applicability is not restricted to monolithic panels, on the contrary, the approach is well suited for sandwich panels with marked thickness-wise heterogeneity. Due to the efficiency of the formulation, the effect of various design parameters, either geometrical or mechanical, can be easily explored. The validation is performed against benchmarks of increasing complexities, namely a single-layer square plate, a shell reinforced by randomly oriented nanotubes, sandwich panels with three distinct configurations. The importance of allowing kinematic descriptions of tunable accuracy within a unique framework is well demonstrated by the proposed assessments.

Keywords: bending, free-vibration, functionally graded, nanotubes, sandwich, sublaminate, variable kinematics.

1 Introduction

Over the last few decades, the aerospace industry has witnessed the rapid advent of composite materials. These have been progressively used to design secondary and primary structures, representing approximately 50% of the structural weight of modern aircraft structures. Exceptional mechanical properties such as high stiffness-to-weight and strength-to-weight ratios, fatigue and corrosion resistance, impact toughness are few but examples of the advantages offered by composites. On top of that, composite materials offer the chance

*Corresponding author. *Email address:* riccardo.vescovini@polimi.it (Riccardo Vescovini)

to tailor the thermo-electro-mechanical properties of the structure by properly designing the reinforcement orientation, stacking sequence, material combination.

Newborn types of composites such as Functionally Graded Materials (FGMs) further extend the design freedom by allowing a continuous variation of material properties along the thickness direction of structural panels. The original idea of FGM can be dated back to mid 1980s [1] with the development of a continuously graded metallic-to-ceramic heat barrier for hypersonic space-planes capable of withstanding extreme temperature gradients without failing due to thermally induced interlaminar stresses.

Since then, FGMs have received increasing interest from the research community regarding: production aspects, see, e.g., the comprehensive review of Ref. [2]; microstructural models for evaluating the elastic properties, [3–5]; structural applications and numerical methods, [6] and [5, 7–11].

The idea of grading the mechanical properties along the thickness can not be straightforwardly extended to composite materials due to the relatively large typical dimensions of conventional fibres with respect to the thickness of the layers. The discovery of Carbon NanoTubes (CNTs) [12, 13] allowed to progressively overcome this limitation.

Despite their outstanding elastic properties, it is well understood that CNTs can not be utilised as structural components, unless they are embedded in a proper supporting medium such as a polymeric matrix. Few examples of Carbon Nanotubes Reinforced Composites (CNTRC) are the epoxy Single Walled Carbon Nanotubes (SWCNT) composites tested by Ajayan et al. [14] and those reported in the reviews [15, 16].

In 2009, the concept of FGM was first applied to CNTRC by Shen [17], who considered a triangular distribution of SWCNT in PmPV and obtained a Functionally Graded Carbon NanoTube Reinforced Composite (FG-CNTRC). In the last decade, several research works were directed toward the assessment of the potential offered by FG-CNTRC in structural applications, as documented by the reviews of Liew et al. [18, 19]. An interesting review covering modelling aspects for FGM plates and shell is found in Ref. [20].

In the present work, a unified approach is adopted that allows to build kinematic models of arbitrary complexity, combining accuracy and efficiency in an optimal balance. The two pillars of the formulation are the sublaminates idealization of the structure and the variable-kinematics formulation.

On the one hand, the discretization in sublaminates allows to implement different kinematic descriptions in the different thickness subregions, independently from each other. The idea is widely used for sandwich beams and panels to confine high-order expansions in the soft core(s), see for exampl [21–24]. Few but significant applications of multiple-kinematics theories to FG panels are found in the recent literature, see for example [25].

On the other hand, the idea of a unified formulation, embedding any arbitrary kinematic model, was proposed by Carrera [26, 27], and is often referred to as Carrera's Unified Formulation (CUF). A generalization of the formulation is the Generalized Unified Formulation [28], allowing different orders of expansions of the displacement components to be accounted for. Many relevant applications of unified formulations to

FG problems can be identified, see for example [29–32].

The unified, variable-kinematics approach and the sublaminate description were merged to achieve the so-called Sublaminate-GUF (SGUF) in Ref. [33]. Successive works [34–37] demonstrated the possibility of achieving an excellent ratio between accuracy and number of degrees of freedom.

To the present, no applications of multiple-and-variable kinematics models to FG panels are reported, therefore the work aims at filling this gap.

2 Theoretical framework

A numerical formulation is developed for multilayered cylindrical shells embedding layers with mechanical properties graded along the thickness direction.

Without loss of generality, a sandwich panel is considered with laminated bottom skin and Functionally Graded (FG) top skin, as illustrated in Figure 1. The panel is characterized by a mid-surface curvature radius R, length a, arclength $b = R\varphi$ and thickness h. The mid-surface is spanned by $x \in [0, a]$ and $y \in [0, b]$ while $z \in [-h/2, h/2]$ runs along the thickness-wise direction.

Free-vibration and bending problems are analysed. In the latter case, pressure loads acting on the inner and/or outer surfaces with arbitrary distribution will be considered as:

$$f_{\text{top}} = f_z^{\text{top}}(x, y, t) \qquad f_{\text{bot}} = f_z^{\text{bot}}(x, y, t) \tag{1}$$

2.1 The Principle of Virtual Displacements

The equilibrium condition is expressed by means of the Principle of Virtual Displacements (PVD), which reads:

$$\int_V \delta\boldsymbol{\varepsilon}^{\mathrm{T}} \boldsymbol{\sigma} \, \mathrm{d}V = -\int_V \delta\mathbf{u}^{\mathrm{T}} \rho \, \ddot{\mathbf{u}} \, \mathrm{d}V + \int_{\Omega_{\text{top}}} \delta u_{\text{top}} f_{\text{top}} \, \mathrm{d}\Omega_{\text{top}} + \int_{\Omega_{\text{bot}}} \delta u_{\text{bot}} f_{\text{bot}} \, \mathrm{d}\Omega_{\text{bot}} \tag{2}$$

Here, $\boldsymbol{\sigma}$ and $\boldsymbol{\varepsilon}$ are the stress and strain vectors, respectively, the double-dot denotes second time derivative, and $u_{\text{bot/top}} = u_z(x, y, \pm h/2)$ are the z-components of the displacement field evaluated at inner and outer surfaces Ω_{top} and Ω_{bot}, respectively. The elementary volume is:

$$\mathrm{d}V = \left(1 + z/R\right) \, \mathrm{d}x \, \mathrm{d}y \, \mathrm{d}z \tag{3}$$

where $\mathrm{d}x \, \mathrm{d}y = \mathrm{d}\Omega$ is the elementary mid-surface.

According to the S-GUF description, the panel is divided into a set of sublaminates, each comprising (one or more) adjacent plies with similar mechanical properties. Sublaminates are numbered from $k = 1$ to $k = N_k$ while plies are numbered locally within each sublaminate from $p = 1$ to $p = N_p^k$. The formulation allows to build multiple-kinematics models (i.e. different theories are adopted in different thickness sub-regions simultaneously, effectively minimizing the number of degrees of freedom) within a variable-kinematics

framework (i.e. a parametric approach that allows to implement a virtually infinite number of kinematic theories in a simple and straightforward manner).

Once a proper kinematic model is postulated, the strain and stress components are obtained from the (unknown) kinematic variables of the model by means of gradient and constitutive laws. In the following, a generic quantity referred to the p-th ply of the k-th sublaminate is written as $()^{p,k}$.

2.2 Constitutive equation for FG materials

Within the framework of linear elasticity, the Hooke's law for orthotropic materials reads:

$$\boldsymbol{\sigma}^{p,k}(x,y,\zeta_p) = \tilde{\mathbf{C}}^{p,k}(\zeta_p)\boldsymbol{\varepsilon}^{p,k}(x,y,\zeta_p) \tag{4}$$

where $\tilde{\mathbf{C}}^{p,k}$ is expressed in the structure reference frame and has at most the following non-null components:

$$\tilde{\mathbf{C}}^{p,k} = \begin{bmatrix} \tilde{C}_{11}^{p,k} & \tilde{C}_{12}^{p,k} & \tilde{C}_{13}^{p,k} & 0 & 0 & \tilde{C}_{16}^{p,k} \\ \tilde{C}_{12}^{p,k} & \tilde{C}_{22}^{p,k} & \tilde{C}_{23}^{p,k} & 0 & 0 & \tilde{C}_{26}^{p,k} \\ \tilde{C}_{13}^{p,k} & \tilde{C}_{23}^{p,k} & \tilde{C}_{33}^{p,k} & 0 & 0 & \tilde{C}_{36}^{p,k} \\ 0 & 0 & 0 & \tilde{C}_{44}^{p,k} & \tilde{C}_{45}^{p,k} & 0 \\ 0 & 0 & 0 & \tilde{C}_{45}^{p,k} & \tilde{C}_{55}^{p,k} & 0 \\ \tilde{C}_{16}^{p,k} & \tilde{C}_{26}^{p,k} & \tilde{C}_{36}^{p,k} & 0 & 0 & \tilde{C}_{66}^{p,k} \end{bmatrix} \tag{5}$$

The elastic coefficients in each FG layer are obtained through an homogenization procedure and are function of the continuous local variable ζ_p that ranges from -1 to $+1$ at the lower and upper interfaces, respectively. Note that the thickness dependence is treated analytically, i.e. the layers are not discretized into sets of mathematical layers.

Once the distribution of the two elementary constituents is known as function of ζ_p, it is possible to determine the effective elastic properties according to either: the rule of mixtures [38, 39], which is applicable for both conventional FGMs and FG-CNTRCs, or the Eshelby-Mori-Tanaka approach [40], specialized here to polymers reinforced by infinitely slender nanotubes [41].

In the case of layers made by nanotubes-reinforced plastics, it is assumed that the volume fraction can be graded at most linearly through the thickness, according to the following distributions, commonly used by most of the authors:

$$\begin{aligned} &\text{UD} \quad : V_r(\zeta_p) = V_r^* \\ &\text{FG-V} : V_r(\zeta_p) = \left(1+\zeta_p\right) V_r^* \\ &\text{FG-A} : V_r(\zeta_p) = \left(1-\zeta_p\right) V_r^* \\ &\text{FG-O} : V_r(\zeta_p) = 2\left(1-|\zeta_p|\right) V_r^* \\ &\text{FG-X} : V_r(\zeta_p) = 2|\zeta_p| V_r^* \end{aligned} \tag{6}$$

where $V_r(\zeta_p)$ is the local reinforcement volumetric fraction and V_r^* is the average value. The matrix volumetric fraction is then:

$$V_m(\zeta_p) = 1 - V_r(\zeta_p) \tag{7}$$

In the case of conventional FGMs, a single-parameter power-law distribution is selected among the many available [11] to describe the microstructural grading between the two constituents. In order to preserve a common notation, and without loss of generality, it will be assumed that one constituent plays the role of the matrix while the other is the reinforcement. Accordingly, the grading is assumed as:

$$\begin{aligned} \text{FGM-V} : V_r(\zeta_p) &= \left(\frac{1+\zeta_p}{2}\right)^n \\ \text{FGM-A} : V_r(\zeta_p) &= \left(\frac{1-\zeta_p}{2}\right)^n \end{aligned} \tag{8}$$

where n ranges from zero to infinity, the two extremes representing a non-graded layer. Few examples of possible distributions that can be described with such laws are shown in Figure 2.

Rule of mixture

According to the rule of mixture, the mean material properties are estimated through a weighted summation of the elastic properties of the two constituents.

When layers' microstructure is graded between two isotropic materials, i.e. conventional FGMs, the rule reads:

$$P = V_r P_r + V_m P_m \tag{9}$$

where P is either the Young's modulus, Poisson's ratio or mass density. The shear modulus is obtained as $G = 0.5E/(1+\nu)$ and is a non-linear function of V_r if both E and ν of the two constituents are different from each other. In practice, it is often assumed that $\nu_r = \nu_m$.

Note, several authors express directly the non-linear relation between the elastic properties and the thickness coordinate [42–44]. The two approaches are clearly equivalent.

In the case of nanotubes, application of the rule of mixture results in drastic overestimation of the elastic properties unless correction factors η_i are introduced to account for the non-ideal load transmission between matrix and fibres. The factors η_i can be determined according to the analytical approach developed in [45] or estimated to match experimental data or molecular dynamics simulations [46]. The extended rule of mixture for FG-CNTRC reads:

$$\begin{aligned} E_1 &= \eta_1 V_r E_1^r + V_m E_m \\ \frac{\eta_2}{E_2} &= \frac{V_r}{E_2^r} + \frac{V_m}{E_m} \\ \frac{\eta_3}{G_{12}} &= \frac{V_r}{G_{12}^r} + \frac{V_m}{G_m} \\ \nu_{12} &= V_r \nu_{12}^r + V_m \nu_m \end{aligned} \tag{10}$$

where E_1 is the Young's modulus in the fibres direction, E_2 is the Young's modulus in directions perpendicular to the fibres, G_{12} is the in-plane shear modulus and ν_{12} is the Poisson's ratio. Assuming transversally isotropic behaviour, $E_3 = E_2$ and $G_{13} = G_{12}$.

In addition, the remaining coefficients can be assumed as $G_{23} = G_{12}$ ($\nu_{23} = \nu_{12}$) or $G_{23} = G_m$ ($\nu_{23} = \nu_m$), depending on the material at hand.

Eshelby-Mori-Tanaka – Randomly oriented CNTs

The Eshelby-Mori-Tanaka method is an advanced approach based on micromechanics of inclusions and defects. The method is applied here to composites reinforced by randomly oriented straight CNTs. Further applications of the method to uniformly aligned, curved, partially or fully agglomerated CNTs can be found in [47].

If nanotubes are randomly dispersed in the matrix, the resulting composite material can be modelled as an equivalent isotropic one, whose elastic coefficients are:

$$E = \frac{9KG}{3K+G} \qquad \nu = \frac{3K-2G}{6K+2G} \tag{11}$$

where K and G are the bulk and shear moduli, computed as:

$$K = K_m + \frac{V_r\left(\delta_r - 3K_m\alpha_r\right)}{3\left(V_m + V_r\alpha_r\right)} \qquad G = G_m + \frac{V_r\left(\eta_r - 2G_m\beta_r\right)}{2\left(V_m + V_r\beta_r\right)} \tag{12}$$

where K_m and G_m are the bulk and shear moduli of the matrix and the remaining coefficients are:

$$\begin{aligned}
\alpha_r &= \frac{3\left(K_m + G_m\right) + k_r - l_r}{3\left(G_m + k_r\right)} \\
\beta_r &= \frac{1}{5}\left[\frac{4G_m + 2k_r + l_r}{3\left(G_m + k_r\right)} + \frac{4G_m}{G_m + p_r} + \frac{2\left[G_m\left(3K_m + G_m\right) + G_m\left(3K_m + 7G_m\right)\right]}{G_m\left(3K_m + G_m\right) + m_r\left(3K_m + 7G_m\right)}\right] \\
\delta_r &= \frac{1}{3}\left[n_r + 2l_r + \frac{\left(2k_r + l_r\right)\left(3K_m + 2G_m - l_r\right)}{G_m + k_r}\right] \\
\eta_r &= \frac{1}{5}\left[\frac{2}{3}\left(n_r - l_r\right) + \frac{8G_m p_r}{G_m + p_r} + \frac{2\left(k_r - l_r\right)\left(2G_m + l_r\right)}{3\left(G_m + k_r\right)} + \frac{8m_r G_m\left(3K_m + 4G_m\right)}{3K_m\left(m_r + G_m\right) + G_m\left(7m_r + G_m\right)}\right]
\end{aligned} \tag{13}$$

where k_r, l_r, m_r, n_r, and p_r are the Hill's elastic moduli of the reinforcing phase [48].

A thorough derivation of the above equations is presented in [41], starting from the results derived in [40].

The density of the composite material is computed by the weighted summation of the constituents densities, which is:

$$\rho = V_r\rho_r + V_m\rho_m \tag{14}$$

2.3 The gradient equations

Preserving the ply-sublaminate notation introduced before, the linear strain-displacement relation for a cylindrical shell reads:

$$\varepsilon_x^{p,k} = \frac{\partial u_x^{p,k}}{\partial x} \tag{15}$$

$$\varepsilon_y^{p,k} = \frac{1}{1+z/R}\left(\frac{\partial u_y^{p,k}}{\partial y} + \frac{u_z^{p,k}}{R}\right) \tag{16}$$

$$\gamma_{xy}^{p,k} = \frac{\partial u_y^{p,k}}{\partial x} + \frac{1}{1+z/R}\frac{\partial u_x^{p,k}}{\partial y} \tag{17}$$

$$\gamma_{yz}^{p,k} = \frac{\partial u_y^{p,k}}{\partial z} + \frac{1}{1+z/R}\left(\frac{\partial u_z^{p,k}}{\partial y} - \frac{u_y^{p,k}}{R}\right) \tag{18}$$

$$\gamma_{xz}^{p,k} = \frac{\partial u_x^{p,k}}{\partial z} + \frac{\partial u_z^{p,k}}{\partial x} \tag{19}$$

$$\varepsilon_z^{p,k} = \frac{\partial u_z^{p,k}}{\partial z} \tag{20}$$

where the flat plate equations are recovered as a special case by setting $1/R = 0$.

2.4 The S-GUF and Ritz approximations

The unknown displacement components are expanded within each ply-sublaminate according to the Sublaminate Generalized Unified Formulation (S-GUF). The approximation is written as:

$$\begin{cases} u_x^{p,k}(x,y,z_p,t) = F_{\beta_{u_x}}(z_p)u_{x\beta_{u_x}}^{p,k}(x,y,t) & \beta_{u_x} = 0,1,\ldots,N_{u_x}^k \\ u_y^{p,k}(x,y,z_p,t) = F_{\beta_{u_y}}(z_p)u_{y\beta_{u_y}}^{p,k}(x,y,t) & \beta_{u_y} = 0,1,\ldots,N_{u_y}^k \\ u_z^{p,k}(x,y,z_p,t) = F_{\beta_{u_z}}(z_p)u_{z\beta_{u_z}}^{p,k}(x,y,t) & \beta_{u_z} = 0,1,\ldots,N_{u_z}^k \end{cases} \tag{21}$$

where $F_{\beta_{u_r}}$ are thickness functions and $N_{u_r}^k$ is the order of expansion of the r-th displacement component within the k-th sublaminate. In the following, $\mathrm{ED}_{N_{u_x},N_{u_y},N_{u_z}}$ means an Equivalent Single Layer (ESL) theory, i.e. the plies of the k-th sublaminate share the same kinematic variables, while $\mathrm{LD}_{N_{u_x},N_{u_y},N_{u_z}}$ is a Layer-Wise (LW) theory of orders N_{u_x}, N_{u_y}, N_{u_z}.

The proposed formulation allows to easily generate any combination of structural theories in different thickness subregions, which is particularly useful in the case of FGMs and FG-CNTRCs. These materials can be combined to generate unconventional configurations, in which case classical theories may fail to produce sufficiently accurate results, as shown later.

Any combination of ED_N and LD_N theories can be considered in the present framework. In this regard, the S-GUF approach can be interpreted as a layerwise formulation with two distinctive features. Firstly, plies are replaced by clusters of plies – mathematical layers or sublaminates. Secondly, each mathematical layer is

associated with a specific kinematic description, in general different from the others. According to the way the theories are formulated and assembled, the proposed approach falls in the paradigm of Carrera's Unified Formulation (CUF). At the same time, the model cannot be uniquely identified referring to the standard notation (ED or LD), but information is necessary regarding which theories are combined along with their order of expansion. For this reason, the notation adopted here considers a sequence of acronyms, ED and LD, expressing the theory associated with each mathematical layer.

The resulting set of two-dimensional differential equations is solved by expanding each unknown generalized displacement component according to the Ritz method as:

$$\begin{cases} u^{p,k}_{x\beta_{u_x}}(x,y,t) = N_{u_x j}(x,y) u^{p,k}_{x\beta_{u_x} j}(t) \\ u^{p,k}_{y\beta_{u_y}}(x,y,t) = N_{u_y j}(x,y) u^{p,k}_{y\beta_{u_y} j}(t) \qquad\qquad j = 1,2,\ldots,M \\ u^{p,k}_{z\beta_{u_z}}(x,y,t) = N_{u_z j}(x,y) u^{p,k}_{z\beta_{u_z} j}(t) \end{cases} \tag{22}$$

where $N_{u_r j}$ are part of a complete set of boundary-compliant shape functions, taken as the product of the simplest bivariate polynomial fulfilling the boundary conditions and a set of Legendre polynomials expanded up to orders R and S, where $M = R \times S$.

The discrete form of the PVD is obtained after integrating the thickness and Ritz functions, either numerically or analytically. The discrete form of the PVD has to be expanded over the theory-related and Ritz indexes, then assembled at ply-sublaminate levels to bring the problem to an easier-to-handle vector equation. Detailed steps can be found in [34] and [37], where the formulation is developed for plates and shells.

3 Results

The formulation is applied here to several test cases of increasing complexity.

The first two benchmarks deal with flat and curved CNTRC single-layer panels. In these cases, the kinematic models are realtively simple, as one single sublaminate is needed for modelling the stack.

The third example deals with a conventional FGM configuration, i.e. a three-layer panel made by metallic, metallo-ceramic and ceramic layers, and is believed of interest due to the availability of exact results to be used for comparison purposes.

The fourth to sixth benchmarks deal with multi-layer sandwich panels, allowing the potential of the formulation to be fully exploited.

3.1 Case study 1 – FG plate

The first example regards the bending and free vibration response of FG-CNTRC plates studied by Zhu et al. [49]. Square plates are considered ($a/b = 1$) with clamped or simply-supported edges. The thickness h is

equal to 2 mm, whilst the width-to-thickness ratios are $b/h = \{10, 20, 50\}$.

The effective material properties of the two-phase nanocomposite, mixture of CNTs with $E_1^r = 5.6466$ TPa, $E_2^r = 7.0800$ TPa, $G_{12}^r = 1.9446$ TPa, $\nu_{12}^r = 0.175$, $\rho_r = 1.4$ g/cm^3 and an isotropic polymer with $E_m = 2.1$ GPa, $\nu_m = 0.34$ $\rho_m = 1.15$ g/cm^3, are estimated through the rule of mixture of Eq. (10), with efficiency parameters:

$$\begin{aligned} &\text{if } \; V_r^* = 0.11 \quad \rightarrow \quad \eta_1 = 0.149 \; , \; \eta_2 = 0.934 \\ &\text{if } \; V_r^* = 0.17 \quad \rightarrow \quad \eta_1 = 0.149 \; , \; \eta_2 = 1.381 \end{aligned} \tag{23}$$

In addition, it is assumed that $\eta_2 = \eta_3$, $G_{23} = G_{13} = G_{12}$ and $\nu_{23} = \nu_{13} = \nu_{12}$.

The first 6 frequency parameters, defined as $\hat{\omega}_i = \frac{a^2}{h}\sqrt{\frac{\rho_m}{E_m}}\omega_i$, are computed by means of a third-order theory $\text{ED}_{3,3,2}$ and 20×20 Ritz functions for several combinations of input parameters. The choice of the kinematic model is based upon a preliminary convergence test, requiring three digits not to change when increasing the number of trial functions. The convergence behaviour with respect to the Ritz expansion was found to be almost independent from the volumetric fraction and thickness distribution of the nanotubes, while being mostly driven by the thickness ratio.

A comprehensive set of results is reported in Table 1 for all the combination of geometrical and material properties and boundary conditions, against those obtained in [49] using Ansys. It can be noted that the frequency associated with the (1,1) mode is the most sensible to variations of the reinforcement pattern. Specifically, the changes are: -16% to -26% between FG-O and UD and $+8\%$ to $+20\%$ between FG-X and UD for the SSSS plate; -8% to -24% between FG-O and UD and $+3\%$ to $+16\%$ between FG-X and UD for the CCCC plate. It worth noting that thinner plates, i.e. $b/h = 50$, are those undergoing the largest variations, which are almost independent on the average reinforcement fraction. The effect of the deposition pattern is less relevant for modes with increasing number of half-waves perpendicular to the fibres direction.

A graphical comparison is presented in Figure 3. In particular, the first six frequencies are illustrated in Figure 3(a) for a thin plate with thickness ratio of 50, average reinforcement fraction 0.11 and several deposition patterns. The fundamental frequency is reported in Figure 3(b) for moderately thick plates with thickness ratio of 10 and several reinforcement fractions and distributions.

Bending results are reported for uniformly distributed pressure load of amplitude $f_0^{\text{top}} = -0.1$ MPa acting on the upper surface.

The normalized transverse displacements $\hat{u}_z = \frac{1E06}{b(b/h)^2} u_z(a/2, b/2, 0)$ are collected in Table 2, where the comparison is reported against the results of [49]. Good agreement is observed, with an average error smaller than 1% and amaximum error below 5%.

The normalized axial stress $\hat{\sigma}_x = \frac{h^2}{|f_0|a^2}\sigma_x$ evaluated through the thickness at $x = a/2$, $y = b/2$ and transverse shear stress $\hat{\tau}_{xz} = \frac{h}{|f_0|a}\tau_{xz}$ evaluated through the thickness at $x = a/4$, $y = b/2$ for width-to-thickness ratio $b/h = 50$ and reinforcement volume fraction $V_{\text{CNT}}^* = 0.17$ are shown in Figures 4 and 5, respectively. Simply supported and clamped boundary conditions are considered. The results are in good

agreement with the ones obtained by Zhu et al. [49], as seen from Figure 4.

Similar patterns are observed for the stresses distributions, irrespective of the boundary condition. The results of Figures 4 and 5 illustrate the possibility of achieving through-the-thickness modulation of the stress field. For instance, the maximum values of the in-plane normal stress of FG-O is located at about one quarter thickness rather than at the outer surfaces as in the case of an homogeneous plate. In addition, the in-plane normal stress for FG-V is non-null at the mid-plane. Furthermore, the FG-X configuration is associated with the lowest maximum shear stress due to a more uniform distribution through-the-thickness.

3.2 Case study 2 – Shells reinforced with randomly oriented CNTs

The second benchmark regards a set of curved panels reinforced by randomly oriented nanotubes. Results were obtained by Sobhani Aragh et al. [50] using the differential quadrature method. The structure is a thick shell with radius-to-thickness ratio $R/h = 10$, angular width $\varphi = \pi/4$, length-to-radius ratio $a/R = \{2, 5, 10\}$. The straight edges are simply supported while the curved edges can be either clamped-clamped or free-clamped. The resin is PMMA whose elastic properties are $E_m = 2.5$ GPa and $\nu_m = 0.34$, while the CNTs are characterized by $E_1^f = 5.6466$ TPa, $E_2^f = 7.0800$ TPa, $G_{12}^f = 1.9446$ TPa, $\nu_{12}^f = 0.175$, $\rho^f = 1.4$ g/cm^3. The nanotubes are randomly oriented and the mean properties of the resulting isotropic composite material are computed referring to the Eshelby-Mori-Tanaka scheme. The kinematic model is $\mathrm{ED}_{3,3,2}$ with 10×10 Ritz functions.

The fundamental frequency parameters, defined as $\Omega_{1,1} = (R/\pi)^2\sqrt{h\rho_m/D_m}\omega_{1,1}$ with $D_m = E_m h^3/(12(1-\nu_m^2))$, are collected in Table 3, for all the possible combinations of geometric and material properties. The drastic sensibility to the volume fraction distribution can be noted by inspection of Table 3. Specifically, the FG-X shell is characterized by a frequency 55% to 70% higher than the FG-O shell. A graphical description is provided in Figure 6 by varying a/R for clamped-clamped, Figure 6(a), or clamped-free, Figure 6(b), curved edges and considering several reinforcement deposition patterns. For small values of the length-to-radius ratio an almost linear reduction of the frequency parameter can be seen in the logarithmic plot of Figure 6. The curve becomes less steep for increasing values of the ratio, reaching, asymptotically, a zero-slope configuration. The frequency parameters become almost independent on the support conditions for $a/R > 4$ because the curved edges become much shorter than the straight ones. A substantial improvement of the fundamental frequency can be ascribed to the FG-X configuration, for every combination of the other parameters, as already observed from the tabulated results and for the flat panel in the previous benchmark.

3.3 Case study 3 – FGM sandwich panel

The third test case deals with the free vibration of curved panels made by an inner metallic layer, an outer ceramic layer and a functionally graded interlayer, allowing a smooth transition of mechanical properties. A

comprehensive set of exact results is reported by Fantuzzi et al. in [51]. This benchmark is considered here for providing evidence of the excellent convergence properties of the proposed formulation.

The geometrical properties of the panels are radius $R = 10$ m, width $b = \pi/3R$, length $a = 20$ m, thickness ratios $R/h = \{1000,\ 100,\ 10,\ 5\}$. The inner layer has relative thickness of 0.15 and is made of aluminum with $E = 73$ GPa, $\nu = 0.3$ and density $\rho = 2800$ kg/m^3. The outer layer is characterized by relative thickness of 0.15 and is made of a ceramic material whose properties are $E = 200$ GPa, $\nu = 0.3$ and $\rho = 5700$ kg/m^3. Two cores are considered: the first is a FGM with ceramic volume fraction varying from zero to one with exponent $p = 0.5,\ 1,\ 2$; the second is a non-graded core with elastic properties equal to the arithmetic average between those of the external layers.

The first ten dimensional frequencies, computed using a third-order layerwise model in conjunction with 15×15 functions, are collected in Table 4. The comparison against reference results reveals agreement up to the third digit. The elastic properties of this configuration are such that the in-plane displacements behave in an almost linear manner along the thickness direction. Therefore, a relatively simple kinematics, e.g. $\text{ED}_{1,1,0}$, suffices in approximating the exact results with errors below 3%.

3.4 Case study 4 – 5-layer FGM sandwich panel

The fourth benchmark deals with the bending of sandwich plates and shells with graded skins. Results were recently obtained by Raissi et al. [52] by means of finite element analyses using three dimensional elements.

The plate is square with dimensions $a = b = 1$ m and thickness ratio $a/h = 20$. The plate is made by two external face sheets with $h_s/h = 0.1$ and composition graded from fully metallic to fully ceramic. The metallic rich sides are bonded to an elastomeric foam core by means of two epoxy adhesive layers with $h_a/h = 0.02$. Mechanical properties of the layers are given in Table 5. The microstructure of the external layers is graded from metallic to ceramic with inhomogeneity coefficient $p = 1$. Beyond this nominal configuration, the effect of geometrical and material properties is assessed by changing one parameter at a time among a/h, h_s/h and p. Simply-supported boundary conditions are considered.

A uniform pressure of amplitude f_0 is applied at the top surface. The response is presented in terms of the nondimensional displacements and stresses $\hat{u}_{\{x,z\}}$, $\hat{\sigma}_x$ and τ_{xz}, defined as:

$$\hat{u}_{\{x,z\}} = \frac{E_{\text{core}} u_{\{x,z\}}}{(1-\nu_{\text{core}}^2) h f_0}, \qquad \hat{\sigma}_x = \frac{\sigma_x}{f_0}, \qquad \hat{\tau}_{xz} = \frac{\tau_{xz}}{f_0} \tag{24}$$

where E_{core} and ν_{core} are the Young's modulus and Poisson's ratio of the elastomeric foam core. Several kinematic models are built, ranging from FSDT up to the layerwise model $\text{LD}_{5,5,4}$. The latter is considered here to demonstrate the ability of the present formulation to obtain quasi-3D predictions. A multiple-kinematics model is built starting from a first-order layerwise description, enriched up to the third-order in the foam core only. The so obtained S-GUF model is therefore $\text{LD}_{1,1,0}$ / $\text{ED}_{3,3,2}$ / $\text{LD}_{1,1,0}$. The Ritz expansion is made by 30×30 functions.

A preliminary comparison between the results obtained by means of four different kinematic theories and the three dimensional finite elements is presented in Figures 7 and 8 in terms of the nondimensional parameters defined in Eq. (24). Note that results obtained using the S-GUF model are almost indistinguishable from the fifth-order layerwise one, despite relying on as little as 19 theory-related degrees of freedom.

The displacements and stresses are evaluated by means of a fifth-order theory $\mathrm{LD}_{5,5,4}$ in several discrete points that are summarized in Table 6, and are collected in Table 7. Overall, good agreement is demonstrated with errors below 5% for most of the entries. Bigger differences are observed when the absolute values of the stress components is relatively small, which could be due to the increased effect of numerical errors. The transverse displacement is predicted with errors below 0.1%.

Note that reducing the plate thickness, i.e. its bending stiffness, has the effect of increasing the transverse displacement and the stresses. On the other hand, increasing the skin-to-total thickness ratio has the effect of reducing both displacement and stresses, although the mean density of the plate gets higher accordingly. Increasing the parameter p has a similar effect to that of reducing the face sheets thickness, although in this case the effect on the transverse shear strain is marginal.

The effect of the inhomogeneity coefficient is further investigated in Figure 9 by presenting additional results in terms of transverse shear stress, membrane normal stress and transverse displacement. With this purpose, a thick plate is considered with $a/h = 10$, $h_s/h = 0.2$ and p ranging from zero (i.e. fully ceramic face sheets) to five. Here and in the following, the kinematic model is $\mathrm{LD}_{1,1,0}$ / $\mathrm{ED}_{3,3,2}$ / $\mathrm{LD}_{1,1,0}$. An increase of p, i.e. shifting to more metallic-rich microstructures, has the effect of reducing the plate bending stiffness as seen from the increased bending deflection. The maximum axial stress increases as well and its pattern becomes highly nonlinear in the face sheets. On the other hand, the structure benefits from a reduction of the transverse shear stress peaks in the face sheets, while a slight increase in the core is observed.

The effect of curving the panel is then studied, varying the width-to-radius ratio (i.e. the angular width) from 0 to $\pi/3$, i.e. from plate to deep shell. The results presented in Figure 10 demonstrate the stabilizing effect of the shell curvature, i.e. the reduced radial displacement, as well as the load redistribution due to increasing values flexural-membrane coupling.

It is interesting to visualize the effects of the inhomogeneity coefficient in the case of a deep shell with $b/R = \pi/3$. As seen from Figure 11, the bending deflection is more than doubled when p is increased from 0 to 5. The transverse shear stress in the outer skin is marginally affected, while it increases drastically in the core and inner face sheet, leading to a significantly different response with respect to plates.

3.5 Case study 5 – Sandwich plate with graded skins

The fifth test case deals with the flexural response of sandwich plates with graded skins. Accurate results were derived by Natarajan et al. [53] using high-order 13-dof, 2D elements enriched with zig-zag functions.

The geometrical properties of the square sandwich plate are: core-to-skin thickness ratio $h_c/h_s = 2$ and

length-to-thickness ratio $a/h = 5$. The plate is simply supported and subjected to bi-sinuisodally distributed pressure load acting on the top surface, as shown in the insert of Figure 12.

The stiff core is made by titanium alloy Ti-6Al-4V with $E_c = 122.56$ GPa, $\nu_c = 0.29$ and mass density $\rho_c = 4.429$ g/cm^3. The skins are made by Poly(methyl methacrylate) with $E_m = 3.52$ GPa, $\nu_m = 0.34$ and $\rho_m = 1150$ kg/m^3, reinforced by CNTs with $E_1^f = 5.6466$ TPa, $E_2^f = 7.0800$ TPa, $G_{12}^f = 1.9446$ TPa, $\nu_{12}^f = 0.175$, $\rho^f = 1.4$ g/cm^3 with volume fraction graded along the thickness with mean value $V_{\rm CNT}^* = 0.17$.

The mean elastic properties are evaluated according to the extended rule of mixtures with coefficients $\eta_1 = 0.142$, $\eta_2 = 1.626$, $\eta_3 = 1.138$. In addition, $G_{23} = 1.2G_{12}$ and $\nu_{23} = \nu_{13} = \nu_{12}$, coherently with the assumptions made in Ref [53].

In the following, the displacements and stress components are normalized as:

$$\hat{u}_x = 10\frac{E_c}{hS^3 f_0}u_x(0,b/2) \qquad \hat{u}_z = \frac{E_c}{hS^4 f_0}u_z(a/2,b/2) \qquad \hat{\sigma}_x = -\frac{1}{S^2 f_0}\sigma_x(a/2,b/2) \qquad \hat{\tau}_{xz} = \frac{1}{S f_0}\tau_{xz}(0,b/2) \tag{25}$$

where $S = a/h$.

A preliminary convergence study is performed to compare different kinematic theories. The results are collected in Table 8, where the comparison is presented against the results of Ref. [53]. The errors are evaluated with respect to $\mathrm{LD}_{5,5,4}$, offering quasi-3D accuracy. A high order Ritz expansion consisting of 25 $\times$ 25 shape functions is selected to guarantee converged results.

It is inferred that high-order ESL models are, in general, not adequate for the analysis of this configuration. Indeed, the abrupt change of material properties at core/skin interfaces are responsible for a piece-wise continuous displacement field.One can observe that the maximum relative error using $\mathrm{ED}_{6,6,5}$ is much higher than $\mathrm{LD}_{1,1,0}$, despite the number of kinematic variables. For the same reason, the accuracy does not improve when enriching the theory from $\mathrm{ED}_{3,3,2}$ to $\mathrm{ED}_{6,6,5}$.

Layerwise models of increasing complexity are also tested. It is observed that any refinement of the kinematic theory beyond $\mathrm{LD}_{3,3,2}$ does not produce relevant accuracy improvements. The proposed S-GUF model is therefore built from $\mathrm{LD}_{3,3,2}$, further simplifying the kinematic description of the stiff core, namely to obtain $\mathrm{ED}_{3,3,2}$ / FSDT / $\mathrm{ED}_{3,3,2}$.

The in-plane and transverse displacements and the in-plane normal and transverse shear stresses are reported in Figures 12 and 13, respectively, where the comparison is presented against reference results.

Due to the relatively large ratio between core and face sheet stiffnesses, high-order theories are needed to appropriately describe the displacement field of the face-sheets, while low-order theories can be used for the core. Therefore, the resulting models are inherently different from those commonly adopted for standard sandwich architectures, such as HSAPT and EHSAPT [24], which are suitable for panels having soft cores and stiff faces.

On the other hand, S-GUF is not bound to any fixed configuration and can always generate a suitable model for any existing and foreseeable structural panel. Coupled with some engineering insight and a few

convergence studies, S-GUF is not only capable of generating a reasonable multiple-kinematics model, but excellent accuracy-to-cost ratio, representing the best alternative to expensive three-dimensional simulations.

3.6 Case study 6 – Sandwich plate with FG core and laminated skins

A novel benchmark is presented to illustrate the potential of the formulation to deal with relatively complex structures that might be of interest for real-life applications. Furthermore, the example is presented to explore the possibility of combining theories of different natures and draw guidelines on how to properly exploit the proposed variable-kinematic approach.

A cantilever sandwich panel is considered with length $a = 300$ mm and width $b = 60$ mm. Skins are quasi-isotropic and are made of 12 kevlar/epoxy plies with thickness of $h_p = 0.15$ mm and lay-up [45/0/-45/90]$_3$. A functionally graded Rohacell core is sandwiched between the two faces, with density and elastic moduli varying with quadratic and quartic laws, respectively. Thick and moderately thick cores are considered with relative thickness $h_c/h_s = \{10, 5\}$, respectively, where $h_s = 12h_p = 1.8$ mm. The configuration is partially inherited from the work of Frostig et al. [54], where the wrinkling response is investigated.

The mechanical properties of the kevlar/epoxy used for the skins are $E_1 = 76$ GPa, $E_2 = 5.5$ GPa, $G_{12} = 2.1$ GPa, $G_{23} = 1.8$ GPa, $\nu_{12} = 0.34$, $\nu_{23} = 0.4$, while those of the Rohacell core are $E_0 = 905.8$ MPa, $G_0 = 370.4$ MPa. The densities are $\rho = 1.380$ g/cm^3 and $\rho_0 = 0.075$ g/cm^3, respectively. Following [54], two different FGM distributions are considered, whose thickness gradings are described by the laws here below:

$$\begin{aligned} &\text{FGM-O}: \quad \rho/\rho_0 = (0.5 - 0.45\zeta_p^2) \qquad E/E_0 = G/G_0 = (0.5 - 0.45\zeta_p^2)^2 \\ &\text{FGM-X}: \quad \rho/\rho_0 = (0.05 + 0.45\zeta_p^2) \qquad E/E_0 = G/G_0 = (0.05 + 0.45\zeta_p^2)^2 \end{aligned}$$

where O and X designate cores that are denser in the middle and external regions, respectively.

The results are presented by illustrating the comparison between the angular frequency computed by means of different theories. Reference results, hereinafter denoted as quasi-3D results, are obtained with a highly refined model with 3 sublaminates (skin/core/skin) and a combination of theories LD$_{5,5,4}$ / ED$_{15,15,14}$ / LD$_{5,5,4}$. Clearly, the model is computationally intensive (383 theory-related DOFs), but proved to guarantee converged results. The Ritz expansion consists of 15 $\times$ 15 shape functions.

To conduct the assessment, a family of equivalent single layer models is generated as ED$_{n,n,n-1}$, with n ranging from 1 to 11. Note, FSDT is recovered as a special case by setting $n = 1$ and using a shear correction factor of 5/6. Sandwich theories are generated in the form ED$_{m,m,m-1}$ / ED$_{n,n,n-1}$ / ED$_{m,m,m-1}$ where m can be either 1 or 3, while n varies from 1 to 11. Note, the kinematic model obtained by setting $m = 1$ and $n = 3$ is similar, but not identical, to the one used in [54], the difference being the adoption of FSDT for the faces instead of the Kirchhoff model. For this reason, this model is indicated next as Sandwich Plate Theory (SAPT) and not EHSAPT as in the referenced paper. In addition, tailored models were considered

by means of ad-hoc combinations of theories, aimed at improving the accuracy to DOFs ratio, as discussed next.

It is worth noting that results do not allow to identify an optimal theory in an absolute sense. On the contrary, the optimality of a theory should be interpreted in terms of error against number of DOFs, i.e. a Pareto front can be identified by retaining the best theory for a fixed amount of DOFs.

The relative error, i.e. $\left(\omega - \omega_{\text{quasi}-3\text{D}}\right)/\omega_{\text{quasi}-3\text{D}}$, is plotted against the number of theory-related DOFs in Figures 14 and 15 for the plates with FGM-O and FGM-X cores, respectively. For clarity, the figures embed the first modal shape and the through-the-thickness modal displacement $\hat{u}_x(a/2, b/2, \zeta)$, which is believed useful for understanding the responses of the two panels investigated.

Clearly, the results are specific for the configurations introduced above. A unique set of guidelines can be hardly provided in spite of the variety of configurations that one may encounter in real-life application. However, a number of features can be highlighted that can be generalized beyond the peculiarities of the examples reported here. Specifically:

- FSDT is recommended as initial guess for modelling faces. In the examples presented here, no improvements can be achieved by enriching the skin kinematics beyond FSDT (Figures 14 and 15);
- in the presence of drastic variations at core/skin interfaces, high-order core descriptions are necessary and the adoption of a sublaminate model in the form skin/core/skin is mandatory. Referring to the proposed examples, one can observe that ED models are responsible for relatively large errors for the FGM-O core (Figure 14);
- if the core is graded such that stiffness mismatch at the core/skin interface is mild, then ED theories can be adequate; referring to the FGM-X core, the accuracy-to-dof ratio of ED models is comparable with that of sandwich theories (Figure 15);
- if the core is characterized by highly nonlinear variations of stiffness and mass properties, models with order higher than the commonly used $\{3, 3, 2\}$ can be necessary at core level. This is particularly true when the variation of properties spans different orders of magnitude, leading to localized effects in the displacement field, as observed from Figures 14 and 15.

In addition to the guidelines drawn above, one may further exploit the potential of the proposed approach starting from a critical assessment of the structure at hand. This step is configuration-dependent, and requires results to be properly interpreted by the analyst, so that models can be optimized on the basis of this. Specializing the discussion to the examples of this section, one can start by observing that displacement field non-linearities are mostly confined in one or two subregions of the core. Therefore, it seems natural to enrich the kinematics in those regions only. An attempt can be made by splitting the core into 3 subdomains. In the case of FG-O grading, five sublaminates can be considered as: top skin, top soft core, stiff core, bottom

soft core, bottom skin. In the case of FG-X grading, three sublaminates can be generated as: top skin and top stiff core, soft core, bottom stiff core and bottom skin. Note, despite the original idea of sublaminates is to group a number of contiguous plies with similar mechanical properties, this concept can be straightforwardly generalized as a valuable mean for improving the modelling capabilities of complex configurations. In the present case, adequate choices for the kinematic theories were found to be $ED_{1,1,0}$ / $ED_{4,4,3}$ / $ED_{1,1,0}$ / $ED_{4,4,3}$ / $ED_{1,1,0}$ and $ED_{1,1,0}$ / $ED_{5,5,4}$ / $ED_{1,1,0}$, for FGM-O and FGM-X, respectively.

The results obtained with the two models are depicted with a green cross in Figures 14 and 15, while the modal displacement is illustrated in Figure 16. Note that, especially in the case of FG-X core, the accuracy-to-dof ratio is located beyond the Pareto optimality front previously identified considering sandwich theories only.

4 Conclusions

The work has regarded the development of a tool for computing the free vibration and bending response of relatively complex two-dimensional structures, characterized by the combined presence of cylindrical curvature and functionally graded layers. A wide class of structures can be analyzed: the formulation can be successfully used for handling thin and thick structures, as well as deep and shallow shells; furthermore, FGM and CNTRC can be studied in the present framework. Material variability along the thickness is modelled with two different approaches, i.e. the rule of mixture and Eshelby-Mori-Tanaka homogenization techniques. No mathematical layers are needed, inasmuch the material dependence on the thickness direction is treated analytically.

The results of the investigation illustrate the capability of the tool to obtain highly refined predictions, with arbitrary accuracy, up to quasi-3D results. This aspect is demonstrated by comparison against reference solutions for frequencies, displacements and stresses. In particular, the ability to accurately predict thickness-wise stress distributions can be relevant for FG structures, where continuous stress modulation can be achieved during the design process.

Furthermore, the case studies illustrate the advantages offered by the S-GUF formulation, allowing any combination of kinematic theory to be straightforwardly generated. Indeed, the inherent flexibility offered by S-GUF allows the computational performance to be optimized through proper definition of the sublaminates and their corresponding theories. This feature is particularly important when dealing with FG structures, where architectures can deviate from conventional stiff face/soft core configurations. In these cases, classical sandwich theories may be inaccurate, while the S-GUF approach offers the required flexibility to generate ad-hoc kinematic models.

References

[1] M. Koizumi. FGM activities in Japan. *Composites Part B: Engineering*, 28(1–2):1–4, 1997.

[2] M. Naebe and K. Shirvanimoghaddam. Functionally graded materials: A review of fabrication and properties. *Applied Materials Today*, 5:223–245, 2016.

[3] T. Reiter, G.J. Dvorak, and V. Tvergaard. Micromechanical models for graded composite materials. *Journal of the Mechanics and Physics of Solids*, 45(8):1281–1302, 1997.

[4] H.M. Yin, L.Z. Sun, and G.H. Paulino. Micromechanics-based elastic model for functionally graded materials with particle interactions. *Acta Materialia*, 52(12):3535–3543, 2004.

[5] D.K. Jha, T. Kant, and R.K. Singh. A critical review of recent research on functionally graded plates. *Composite Structures*, 96:833–849, 2013.

[6] H.S. Shen. *Functionally Graded Materials: Nonlinear Analysis of Plates and Shells*. CRC Press, Boca Raton, 1st edition, 2009.

[7] V. Birman and L.W. Byrd. Modeling and analysis of functionally graded materials and structures. *Applied Mechanics Reviews*, 60(5):195–216, 2007.

[8] P. Marzocca, S.A. Fazelzadeh, and M. Hosseini. A review of nonlinear aero-thermo-elasticity of functionally graded panels. *Journal of Thermal Stresses*, 34(5–6):536–568, 2011.

[9] K. Swaminathan, D.T. Naveenkumar, A.M. Zenkour, and E. Carrera. Stress, vibration and buckling analyses of fgm plates–A state-of-the-art review. *Composite Structures*, 120:10–31, 2015.

[10] F. Xu, X. Zhang, and H. Zhang. A review on functionally graded structures and materials for energy absorption. *Engineering Structures*, 171:309–325, 2018.

[11] A.S. Sayyad and Y.M. Ghugal. Modeling and analysis of functionally graded sandwich beams: a review. *Mechanics of Advanced Materials and Structures*, 26(21):1776–1795, 2019.

[12] S. Iijima. Helical microtubules of graphitic carbon. *Nature*, 354:56–58, 1991.

[13] S. Iijima and T. Ichihashi. Single-shell carbon nanotubes of 1-nm diameters. *Nature*, 363:603–605, 1993.

[14] P.M. Ajayan, L.S. Schadler, C. Giannaris, and A. Rubio. Single-walled carbon nanotube-polymer composites: Strength and weakness. *Advanced Materials*, 12:750–753, 2000.

[15] P.J.F. Harris. Carbon nanotube composites. *International Materials Reviews*, 49(1):31–43, 2004.

[16] K.T. Lau and D. Hui. The revolutionary creation of new advanced materials – carbon nanotube composites. *Composites: Part B*, 33:263–277, 2002.

[17] H.S. Shen. Nonlinear bending of functionally graded carbon nanotube-reinforced composite plates in thermal environments. *Composite Structures*, 91:9–19, 2009.

[18] K.M. Liew, Z.X. Lei, and L.W. Zhang. Mechanical analysis of functionally graded carbon nanotube reinforced composites: A review. *Composite Structures*, 120:90–97, 2015.

[19] K.M. Liew, Z. Pan, and L.W. Zhang. The recent progress of functionally graded CNT reinforced composites structures. *Science Chine Physics, Mechanics & Astronomy*, 63(234601):–, 2020.

[20] H.T. Thai and S.E. Kim. A review of theories for the modeling and analysis of functionally graded plates and shells. *Composite Structures*, 128:70–86, 2015.

[21] Y. Frostig, M. Baruch, O. Vilnay, and I. Sheinman. High-order theory for sandwich-beam behavior with transversely flexible core. *Journal of Engineering Mechanics*, 118:1026–1043, 1992.

[22] P.F. Pai and A.N. Palazotto. A higher-order sandwich plate theory accounting for 3-D stresses. *International Journal of Solids and Structures*, 38(30):5045–5062, 2001.

[23] C.N. Phan, Y. Frostig, and G.A. Kardomateas. Analysis of sandwich beams with a compliant core and with in-plane rigidity-extended high-order sandwich panel theory versus elasticity. *Journal of Applied Mechanics*, 79(4):041001, 2012.

[24] L.A. Carlsson and G.A. Kardomateas. High-order sandwich panel theories. In *Structural and Failure Mechanics of Sandwich Composites*, volume 121 of *Solid Mechanics and Its Applications*, chapter 6. Springer, Dordrecht, 2011.

[25] S. Pandey and S. Pradyumma. Analysis of functionally graded sandwich plates using a higher-order layerwise theory. *Composites Part B: Engineering*, 153:325–336, 2018.

[26] E. Carrera. A class of two-dimensional theories for anisotropic multilayered plates analysis. *Atti Accademia delle Scienze di Torino. Memorie Scienze Fisiche*, 19:1–39, 1995.

[27] E. Carrera. Theories and finite elements for multilayered plates and shells: A unified compact formulation with numerical assessment and benchmarking. *Archives of Computational Methods in Engineering*, 10(3):215–296, 2003.

[28] L. Demasi. ∞^6 Mixed plate theories based on the Generalized Unified Formulation. Part I: Governing equations. *Composite Structures*, 87(1):1–11, 2009.

[29] E. Carrera, S. Brischetto, and A. Robaldo. Variable kinematic model for the analysis of functionally graded material plates. *AIAA Journal*, 46(1):194–203, 2008.

[30] E. Carrera, S. Brischetto, M. Cinefra, and M. Soave. Effects of thickness stretching in functionally graded plates and shells. *Composites Part B: Engineering*, 42(2):123–133, 2011.

[31] L. Dozio. Natural frequencies of sandwich plates with FGM core via variable-kinematic 2-D ritz models. *Composite Structures*, 96:561–568, 2013.

[32] L. Dozio. Exact free vibration analysis of Lévy FGM plates with higher-order shear and normal deformation theories. *Composite Structures*, 111:415–425, 2014.

[33] M. D'Ottavio. A Sublaminate Generalized Unified Formulation for the analysis of composite structures. *Composite Structures*, 142:187–199, 2016.

[34] M. D'Ottavio, L. Dozio, R. Vescovini, and O. Polit. Bending analysis of composite laminated and sandwich structures using sublaminate variable-kinematic Ritz models. *Composite Structures*, 155:45–62, 2016.

[35] R. Vescovini, M. D'Ottavio, L. Dozio, and O. Polit. Thermal buckling response of laminated and sandwich plates using refined 2-D models. *Composite Structures*, 176:313–328, 2017.

[36] R. Vescovini, M. D'Ottavio, L. Dozio, and O. Polit. Buckling and wrinkling of anisotropic sandwich plates. *International Journal of Engineering Science*, 130:136–156, 2018.

[37] A. Gorgeri, R. Vescovini, and L. Dozio. Analysis of multiple-core sandwich cylindrical shells using a sublaminate formulation. *Composite Structures*, 225(111067), 2019.

[38] A.M.K. Esawi and M.M. Farag. Carbon nanotube reinforced composites: Potential and current challenges. *Materials & Design*, 28(9):2394–2401, 2007.

[39] L. Librescu, S.Y. Oh, and O. Song. Thin-walled beams made of functionally graded materials and operating in a high temperature environment: vibration and stability. *Journal of Thermal Stresses*, 28(6–7):649–712, 2008.

[40] T. Mori and K. Tanaka. Average stress in matrix and average elastic energy of materials with misfitting inclusions. *Acta Metallurgica*, 21(5):571–574, 1973.

[41] S. Dong-Li, F. Xi-Qiao, Yonggang Y. H., H. Keh-Chih, and G. Huajian. The effect of nanotube waviness and agglomeration on the elastic property of carbon nanotube-reinforced composites. *Journal of Engineering Materials and Technology*, 126(3):250–257, 2004.

[42] E. Carrera, S. Brischetto, M. Cinefra, and M. Soave. Refined and advanced models for multilayered plates and shells embedding functionally graded material layers. *Mechanics of Advanced Materials and Structures*, 17(8):603–621, 2010.

[43] A.M. Zenkour. Generalized shear deformation theory for bending analysis of functionally graded plates. *Applied Mathematical Modelling*, 30:67–84, 2006.

[44] G.N. Praveen and J.N. Reddy. Nonlinear transient thermoelastic analysis of functionally graded ceramic-metal plates. *International Journal of Solid Structures*, 35(33):4457–4476, 1998.

[45] J.N. Coleman, U. Khan, W.J. Blau, and Y.L. Gun'Ko. Small but strong: A review of the mechanical properties of carbon nanotube–polymer composites. *Carbon*, 44(9):1624–1652, 2006.

[46] Y. Han and J. Elliot. Molecular dynamics simulations of the elastic properties of polymer/carbon nanotube composites. *Computational Materials Science*, 39(2):315–323, 2007.

[47] F. Tornabene, N. Fantuzzi, and E. Viola. Effect of agglomeration on the natural frequencies of functionally graded carbon nanotube-reinforced laminated composite doubly-curved shells. *Composites Part B: Engineering*, 89:187–218, 2016.

[48] R. Hill. A self-consistent mechanics of composite materials. *Journal of the Mechanics and Physics of Solids*, 13(4):213–222, 1965.

[49] P. Zhu, Z.X. Lei, and K.M. Liew. Static and free vibration analyses of carbon nanotube-reinforced composite plates using finite element method with first order shear deformation plate theory. *Composite Structures*, 94(4):1450–1460, 2012.

[50] B. Sobhani Aragh, A.H. Nasrollah Barati, and H. Hedayati. Eshelby-Mori-Tanaka approach for vibrational behavior of continuously graded carbon nanotube-reinforced cylindrical panels. *Composites Part B*, 43(4):1943–1954, 2012.

[51] N. Fantuzzi, S. Brischetto, F. Tornabene, and E. Viola. 2D and 3D shell models for the free vibration investigation of functionally graded cylindrical and spherical panels. *Composite Structures*, 154:573–590, 2016.

[52] H. Raissi, M. Shishehsaz, and S. Moradi. Stress distribution in a five-layer sandwich plate with FG face sheets using layerwise method. *Mechanics of Advanced Materials and Structures*, 26(14):1234–1244, 2019.

[53] S. Natarajan, M. Haboussi, and M. Ganapathi. Application of higher-order structural theory to bending and free vibration analysis of sandwich plates with CNT reinforced composite facesheets. *Composite Structures*, 113:197–207, 2014.

[54] Y. Frostig, V. Birman, and G.A. Kardomateas. Non-linear wrinkling of sandwich panel with functionally graded core – Extended high-order approach. *International Journal of Solids and Structures*, 148–149:122–139, 2018.

Table 1: Effects of width-to-thickness ratio and CNT volume fraction on the non-dimensional natural frequencies $\hat{\omega}_{i,j} = \frac{a^2}{h}\sqrt{\frac{\rho_m}{E_m}}\omega_{i,j}$ for simply supported and clamped CNTRC square plates.

			SSSS				CCCC			
V_r^*	b/h	Mode	UD	FG-V	FG-O	FG-X	UD	FG-V	FG-O	FG-X
0.11	10	(1,1)	13.560	12.304	11.329	14.685	18.052	17.180	16.431	18.603
		(1,2)	17.692	16.943	16.111	18.643	23.314	22.781	22.084	23.893
		(1,3)	27.258	26.979	26.193	28.130	33.411	33.195	32.523	34.040
		(1,4)	40.800	40.801	39.994	41.688	46.801	46.804	46.157	47.461
		(2,1)	32.973	30.862	29.239	34.207	34.888	33.214	31.978	35.802
		(2,2)	35.069	33.361	31.877	36.207	38.115	36.788	35.638	38.996
	20	(1,1)	17.314	14.998	13.393	19.913	28.569	25.985	23.954	30.743
		(1,2)	21.416	19.757	18.332	23.686	33.176	31.149	29.281	35.218
		(1,3)	31.873	31.001	29.629	33.836	43.952	42.676	40.906	45.910
		(1,4)	48.427	48.103	46.556	50.385	60.752	60.099	58.268	62.774
		(2,1)	52.257	46.752	42.655	56.977	59.804	55.349	51.884	62.966
		(2,2)	54.240	49.214	45.316	58.739	62.525	58.493	55.170	65.582
	50	(1,1)	19.155	16.183	14.239	22.902	39.509	33.809	29.920	45.988
		(1,2)	23.270	21.007	19.248	26.630	43.559	38.590	34.968	49.669
		(1,3)	34.038	32.716	31.004	36.939	53.745	50.023	46.684	59.267
		(1,4)	51.902	51.284	49.296	54.740	71.327	68.855	65.538	76.411
		(2,1)	70.019	59.271	52.132	82.323	97.093	84.319	75.287	110.012
		(2,2)	72.127	61.882	54.941	84.148	99.430	87.162	78.353	112.094
0.17	10	(1,1)	16.843	15.294	14.089	18.190	22.527	21.524	20.644	23.179
		(1,2)	22.046	21.175	19.980	23.370	29.124	28.578	27.583	30.012
		(1,3)	34.047	33.827	32.472	35.556	41.766	41.668	40.529	42.931
		(1,4)	51.006	51.208	49.658	52.759	58.522	58.760	57.546	59.872
		(2,1)	41.111	38.624	36.805	42.409	43.548	41.648	40.308	44.579
		(2,2)	43.749	41.787	40.023	45.054	47.595	46.153	44.779	48.728
	20	(1,1)	21.400	18.509	16.507	24.610	35.508	32.320	29.839	38.104
		(1,2)	26.581	24.566	22.596	29.580	41.308	38.873	36.373	43.986
		(1,3)	39.732	38.785	36.541	42.768	54.841	53.435	50.693	57.858
		(1,4)	60.490	60.328	57.473	64.027	75.899	75.381	72.170	79.496
		(2,1)	64.866	58.030	53.083	70.422	74.474	69.096	65.072	78.057
		(2,2)	67.374	61.175	56.357	72.761	77.897	73.083	69.082	81.510
	50	(1,1)	23.607	19.898	17.475	28.275	48.787	41.651	36.839	56.791
		(1,2)	28.810	26.045	23.650	33.193	53.912	47.763	43.060	61.665
		(1,3)	42.367	40.870	38.141	46.652	66.764	62.295	57.500	74.277
		(1,4)	64.783	64.279	60.685	69.661	88.877	86.113	80.746	96.584
		(2,1)	86.385	72.919	64.137	101.542	120.133	104.128	93.071	135.861
		(2,2)	89.052	76.258	67.599	103.956	123.089	107.767	96.846	138.621

Table 2: Effects of width-to-thickness ratio and CNT volume fraction on the non-dimensional transverse displacement $\hat{u}_z = \frac{u_z(a/2,b/2,0)}{b^3/h^2} \times 10^6$ for square plates subjected to a uniform pressure load $f_0^{\text{top}} = -0.1$ MPa.

			SSSS		CCCC		SCSC		SFSF	
V_r^*	b/h		Ref. [49]	S-GUF	Ref. [49]	S-GUF	Ref. [49]	S-GUF	Ref. [49]	S-GUF
0.11	10	UD	3.739	3.711	2.227	2.120	3.325	3.293	3.445	3.414
		FG-V	4.461	4.562	2.351	2.362	3.848	3.902	4.188	4.289
		FG-O	5.216	5.414	2.506	2.599	4.422	4.528	4.960	5.168
		FG-X	3.176	3.138	2.104	1.986	2.864	2.831	2.909	2.864
	20	UD	4.536	4.535	1.673	1.644	4.244	4.236	4.176	4.179
		FG-V	6.095	6.165	1.989	2.030	5.469	5.515	5.684	5.751
		FG-O	7.670	7.806	2.320	2.418	6.715	6.799	7.232	7.370
		FG-X	3.379	3.370	1.438	1.401	3.232	3.226	3.113	3.101
	50	UD	9.240	9.252	2.094	2.097	8.800	8.795	8.544	8.568
		FG-V	13.22	13.26	2.922	2.951	12.02	12.05	12.33	12.38
		FG-O	17.20	17.32	3.764	3.832	15.22	15.29	16.20	16.33
		FG-X	6.332	6.331	1.520	1.513	6.186	6.186	5.889	5.887
0.17	10	UD	2.394	2.377	1.411	1.345	2.124	2.105	2.207	2.189
		FG-V	2.861	2.920	1.483	1.486	2.458	2.488	2.693	2.752
		FG-O	3.368	3.456	1.591	1.624	2.858	2.898	3.202	3.296
		FG-X	2.011	2.026	1.316	1.267	1.802	1.812	1.845	1.853
	20	UD	2.936	2.936	1.070	1.053	2.739	2.735	2.703	2.706
		FG-V	3.964	4.006	1.275	1.299	3.539	3.564	3.704	3.744
		FG-O	5.009	5.076	1.494	1.538	4.384	4.421	4.724	4.792
		FG-X	2.172	2.189	0.9106	0.9053	2.066	2.081	2.000	2.012
	50	UD	6.017	6.026	1.359	1.361	5.712	5.711	5.561	5.580
		FG-V	8.648	8.685	1.909	1.927	7.824	7.842	8.080	8.117
		FG-O	11.29	11.36	2.463	2.497	9.984	10.02	10.63	10.71
		FG-X	4.113	4.124	0.9816	0.9855	3.994	4.005	3.818	3.827

Table 3: Frequency parameter associated with the mode having one by one half-waves, $\Omega_{1,1} = (R/\pi)^2\sqrt{h\rho_m/D_m}\omega_{1,1}$, for several combination of boundary conditions, geometrical, material properties.

		UD		FG-V		FG-A		FG-O		FG-X	
BCs	a/R	Ref. [50]	Present	Ref. [50]	Present	Ref. [50]	Present	Ref. [50]	Present	Ref. [50]	Present
CSCS	2	—	12.9739	10.9280	10.9641	11.4262	11.4442	10.4184	9.9472	16.1171	15.4140
	5	—	10.2376	8.2904	8.3270	8.8180	8.8316	7.9288	7.3864	13.1674	12.5095
	10	—	9.9689	8.0390	8.0756	8.5711	8.5839	7.6971	7.1489	12.8637	12.2122
FSCS	2	—	10.2997	8.3574	8.3888	—	8.8818	—	7.4414	13.2169	12.5710
	5	—	9.9316	7.9497	8.0446	—	8.5509	—	7.1214	12.8101	12.1660
	10	—	9.9002	7.9719	8.0167	—	8.5240	—	7.0963	12.7723	12.1311

Table 4: First ten natural frequencies (Hz) of a simply supported sandwich shell with FGM core.

		Homogeneous core		$p = 0.5$		$p = 1$		$p = 2$	
R/h	Mode	Exact	S-GUF	Exact	S-GUF	Exact	S-GUF	Exact	S-GUF
5	(1,1) - I	51.41	51.42	49.97	49.98	49.72	49.73	49.90	49.91
	(1,0) - II	88.27	88.27	89.54	89.54	88.51	88.51	87.25	87.25
	(2,1) - I	92.81	92.82	91.02	91.02	90.34	90.34	90.16	90.17
	(3,1) - I	146.7	146.7	144.1	144.1	142.8	142.8	142.1	142.1
	(1,2) - I	159.6	159.7	155.8	155.9	154.3	154.3	153.6	153.6
	(0,1) - II	166.4	166.4	167.9	167.9	165.3	165.3	162.4	162.4
	(2,0) - II	176.5	176.5	179.1	179.1	177.0	177.0	174.5	174.5
	(2,2) - I	186.1	186.1	182.3	182.3	180.3	180.3	179.1	179.1
	(1,1) - II	193.4	193.4	195.4	195.4	192.5	192.5	189.3	189.3
	(4,1) - I	209.7	209.8	206.6	206.6	204.4	204.4	202.7	202.8
10	(1,1) - I	31.32	31.32	30.69	30.69	30.54	30.54	30.62	30.62
	(2,1) - I	63.24	63.24	62.56	62.56	62.09	62.09	61.88	61.88
	(1,0) - II	92.19	88.07	89.05	89.04	88.20	88.20	86.87	86.87
	(1,2) - I	88.07	92.20	89.30	89.30	88.80	88.80	89.50	89.51
	(3,1) - I	97.83	97.83	96.35	96.35	95.67	95.67	95.49	95.49
	(2,2) - I	110.5	110.5	107.0	107.0	106.6	106.7	107.3	107.3
	(4,1) - I	137.1	137.1	134.4	134.4	133.5	133.5	133.5	133.5
	(3,2) - I	141.0	141.0	137.0	137.0	136.4	136.4	136.9	136.9
	(0,1) - II	167.0	167.0	168.9	168.9	166.5	166.5	163.7	163.7
	(2,0) - II	176.1	176.1	178.6	178.6	176.4	176.4	173.7	173.7
100	(1,2) - I	11.37	11.37	11.07	11.07	11.04	11.04	11.12	11.12
	(1,1) - I	18.51	18.51	18.74	18.74	18.50	18.50	18.21	18.21
	(1,3) - I	21.99	21.99	21.14	21.14	21.16	21.16	21.47	21.47
	(2,2) - I	22.44	22.44	22.42	22.42	22.21	22.21	22.04	22.04
	(2,3) - I	25.68	25.68	24.86	24.86	24.84	24.84	25.10	25.10
	(3,3) - I	33.18	33.18	32.48	32.48	32.35	32.35	32.48	32.49
	(3,2) - I	37.15	37.15	37.10	37.10	36.92	36.92	36.51	36.52
	(1,4) - I	38.61	38.61	37.33	37.33	37.14	37.14	37.69	37.69
	(2,4) - I	40.93	40.93	39.37	39.37	39.40	39.40	39.96	39.96
	(4,3) - I	43.13	43.13	42.51	42.51	42.26	42.26	42.27	42.27
1000	(1,3) - I	3.436	3.436	3.410	3.409	3.384	3.384	3.371	3.371
	(1,4) - I	4.157	4.157	4.022	4.022	4.020	4.020	4.063	4.063
	(1,2) - I	5.785	5.785	5.854	5.854	5.779	5.779	5.692	5.693
	(1,5) - I	6.113	6.114	5.880	5.880	5.887	5.887	5.970	5.971
	(2,4) - I	7.054	7.054	7.027	7.026	6.966	6.966	6.924	6.925
	(2,5) - I	7.288	7.289	7.106	7.106	7.087	7.087	7.132	7.133
	(1,6) - I	8.706	8.708	8.365	8.367	8.377	8.379	8.501	8.504
	(2,6) - I	9.266	9.268	8.942	8.944	8.944	8.946	9.054	9.056
	(2,3) - I	10.02	10.02	10.12	10.12	9.997	9.997	9.855	9.855
	(3,5) - I	10.41	10.41	10.33	10.33	10.25	10.25	10.21	10.21

Table 5: Mechanical properties of the 5-layer shell.

Sheet type		Mechanical properties	
Face sheet:	Al:	$E_m = 70$ GPa,	$\nu_m = 0.3$
	Al_2O_3:	$E_c = 380$ GPa,	$\nu_c = 0.3$
Epoxy adhesive:		$E = 3.664$ GPa,	$\nu = 0.3$
Foam core:		$E = 1.5$ GPa,	$\nu = 0.463$

Table 6: Coordinates of the evaluation points for the displacement and stress components.

Point number	1	2	3	4	5	6	7
Located at the:	Core	Face sheet	Face sheet	Adhesive	Adhesive	Adhesive	Adhesive
x-coord:	$a/2$	$a/2$	$a/2$	$a/2$	$a/2$	$a/2$	$a/2$
y-coord:	$b/2$	$b/2$	$b/2$	$b/2$	$b/2$	0	0
z-coord:	0	$h/2$	$h/2 - h_s$	$h/2 - h_s$	$h_c/2$	$h/2 - h_s$	$h_c/2$

Table 7: Effect of thickness ratios and degree of inhomogeneity on stresses and displacements for a simply supported 5-layer square plate subjected to uniform pressure load (coordinates of evaluations points in Table 6).

				$\hat{u}_z$	$\hat{\sigma}_x$				$\hat{\tau}_{xz}$		
a/h	h_s/h	p		Point 1	Point 2	Point 3	Point 4	Point 5	Max[a]	Point 6	Point 7
20	0.10	1	Ref. [52]	215.71	388.83	52.505	3.3380	3.1130	7.7091	6.8244	6.8177
			$LD_{5,5,4}$	215.64	390.80	49.733	2.9836	2.7773	7.9985	6.8209	6.7988
15	0.10	1	Ref. [52]	92.599	224.53	27.405	1.7005	1.5445	6.4038	5.0129	4.9987
			$LD_{5,5,4}$	92.548	226.77	25.545	1.7176	1.5745	6.6021	5.0093	4.9833
30	0.10	1	Ref. [52]	813.02	855.22	126.56	7.0285	6.6055	10.554	10.451	10.441
			$LD_{5,5,4}$	812.88	859.85	118.84	6.6010	6.2138	10.987	10.377	10.363
20	0.15	1	Ref. [52]	177.43	294.95	29.602	1.7740	1.5995	7.9822	6.9192	6.9104
			$LD_{5,5,4}$	177.33	295.59	27.340	1.7953	1.6354	8.2574	6.9104	6.8944
20	0.20	1	Ref. [52]	153.54	249.37	19.169	1.3070	1.1630	8.3458	6.9669	6.9587
			$LD_{5,5,4}$	153.43	250.41	14.931	1.1280	0.9958	8.4536	6.9591	6.9463
20	0.10	0.5	Ref. [52]	197.49	335.02	41.210	2.5550	2.3555	7.7714	6.8343	6.8312
			$LD_{5,5,4}$	197.22	329.21	40.436	2.5056	2.3228	8.1594	6.8253	6.8102
20	0.10	2	Ref. [52]	246.57	496.90	63.433	4.1900	3.9230	7.4182	6.8117	6.8030
			$LD_{5,5,4}$	246.48	491.94	64.730	3.7644	3.5191	7.8027	6.8123	6.7842

[a]: maximum value in the upper face sheet.

Table 8: Displacement and stress components of a simply supported sandwich plate with FG skins loaded with bi-sinusoidally distributed pressure. Comparison between different ESL and LW theories and S-GUF model $ED_{3,3,2}$ / FSDT / $ED_{3,3,2}$.

Model	HSDT9	HSDT13	$ED_{1,1,0}$	$ED_{3,3,2}$	$ED_{6,6,5}$	$LD_{1,1,0}$	$LD_{3,3,2}$	$LD_{4,4,3}$	$LD_{5,5,4}$	S-GUF
DOFs			5	11	20	9	27	36	45	21
$\hat{u}_x$	0.6883	0.5463	0.9438	0.7325	0.7366	0.6047	0.6910	0.6911	0.6911	0.6921
$\hat{u}_z$	0.0847	0.1036	0.0760	0.0798	0.0799	0.1000	0.1023	0.1023	0.1023	0.1032
$\hat{\sigma}_x$	0.5747	0.4476	0.7084	0.5519	0.5554	0.4587	0.5242	0.5233	0.5235	0.5250
$\hat{\tau}_{xz}$	0.3926	0.4021	0.3794	0.3922	0.3872	0.3946	0.3928	0.3928	0.3930	0.3930
Max relative error:			37%	22%	22%	13%	0.13%	0.05%	-	0.88%

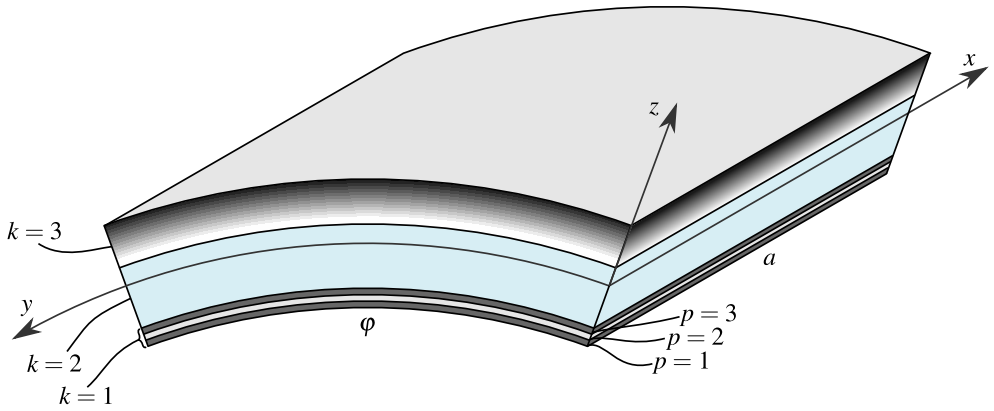

Figure 1: Sketch of a multi-layered cylindrical panel embedding functionally graded layers. Highlighted is an ideal ply-sublaminate discretization according to S-GUF.

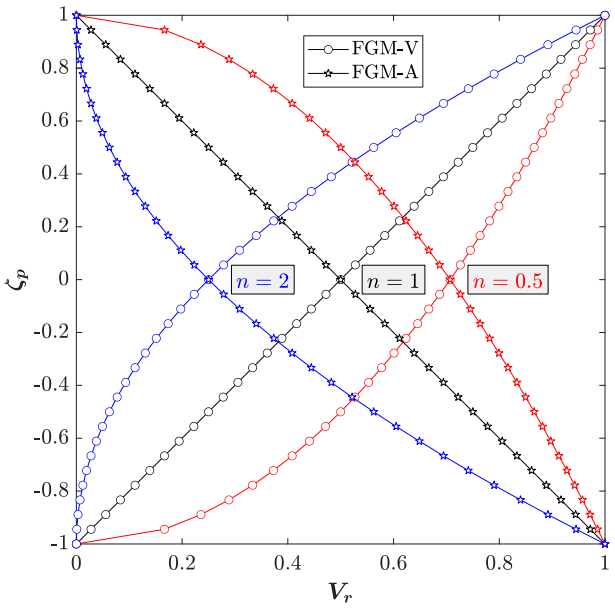

Figure 2: Microstructural gradings using a one-parameter power-law.

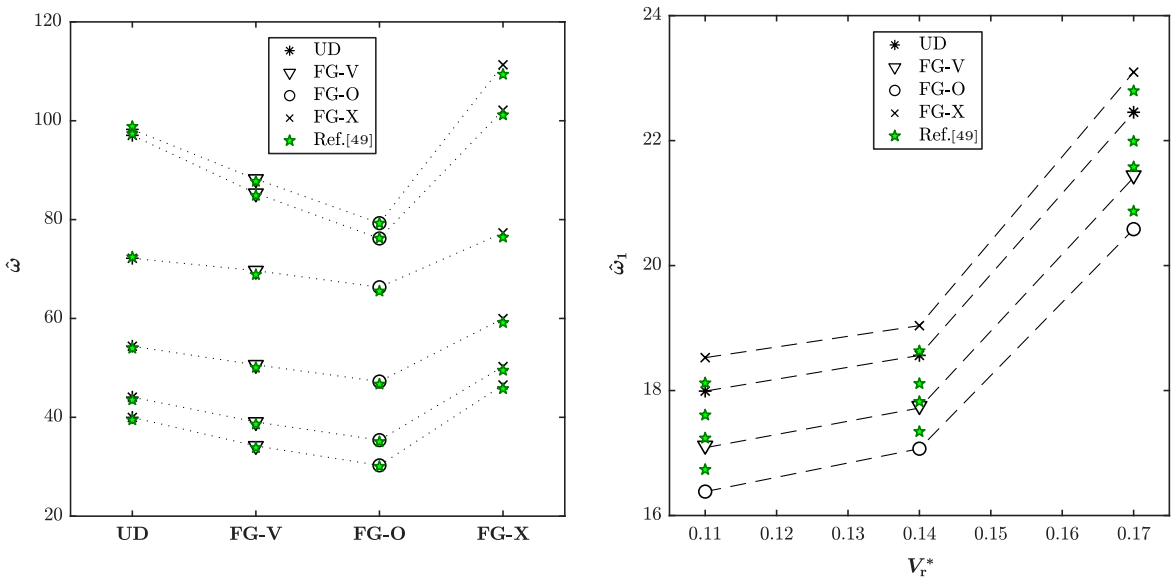

(a) (b)

Figure 3: Frequency parameters $\hat{\omega}_i = \frac{a^2}{h}\sqrt{\frac{\rho_m}{E_m}}\omega_i$ for simply supported square plates with $h = 2$ mm and: (a) $b/h = 50$, $V_r^* = 0.11$; (b) $b/h = 10$.

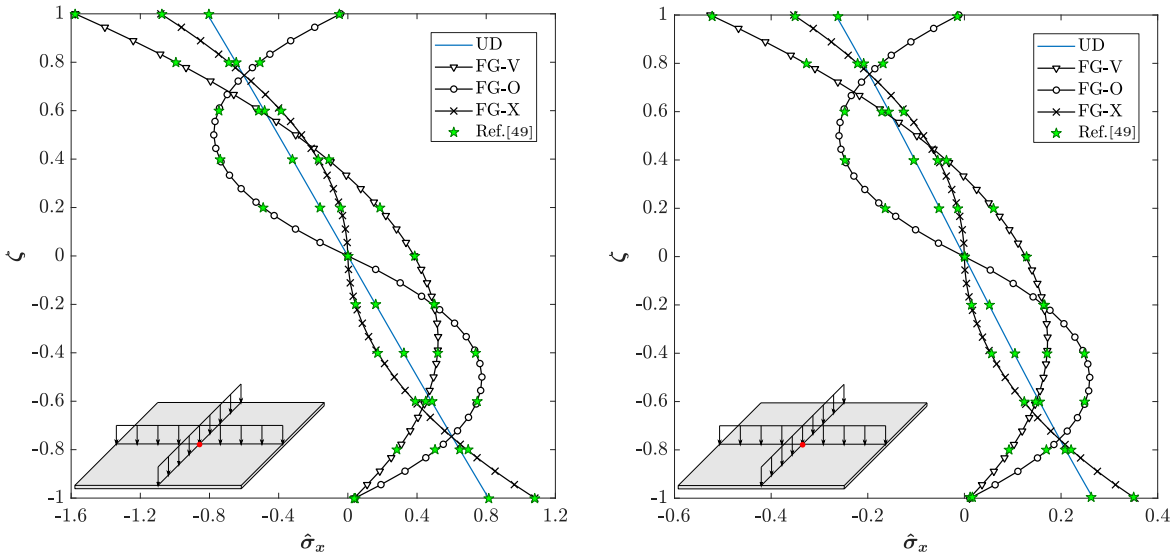

Figure 4: Non-dimensional in-plane normal stress $\hat{\sigma}_x(a/2, b/2, \zeta)$ in a FG-CNTRC plate with $a/h = 50$, $V_r^* = 0.17$ and several reinforcement patterns: (a) simply supported; (b) clamped.

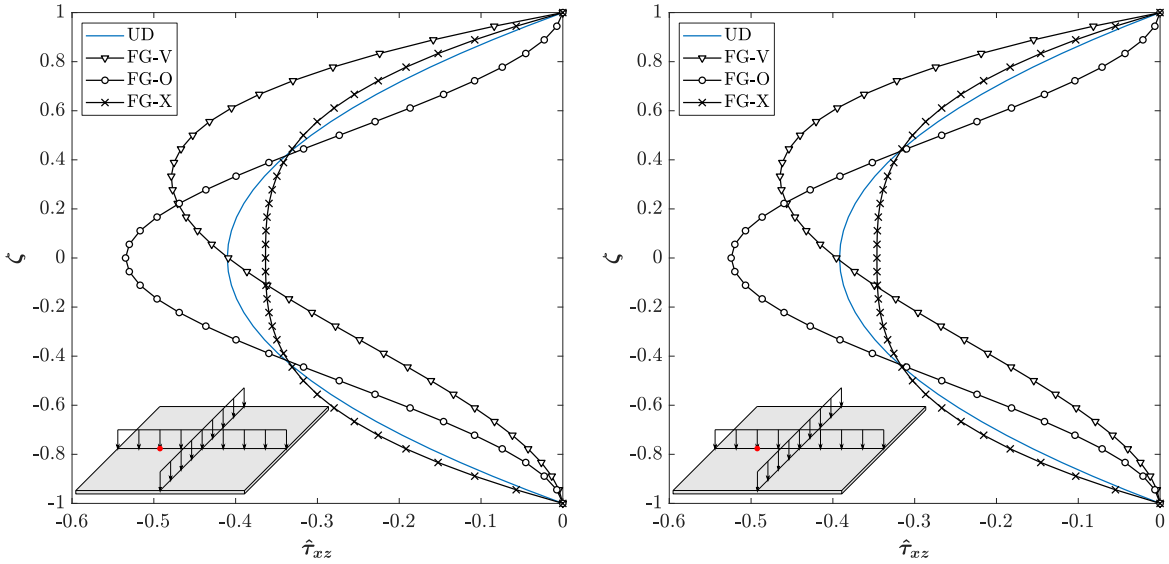

Figure 5: Non-dimensional transverse shear stress $\hat{\tau}_{xz}(a/4, b/2, \zeta)$ in a FG-CNTRC plate with $a/h = 50$, $V_r^* = 0.17$ and several reinforcement patterns: (a) simply supported; (b) clamped.

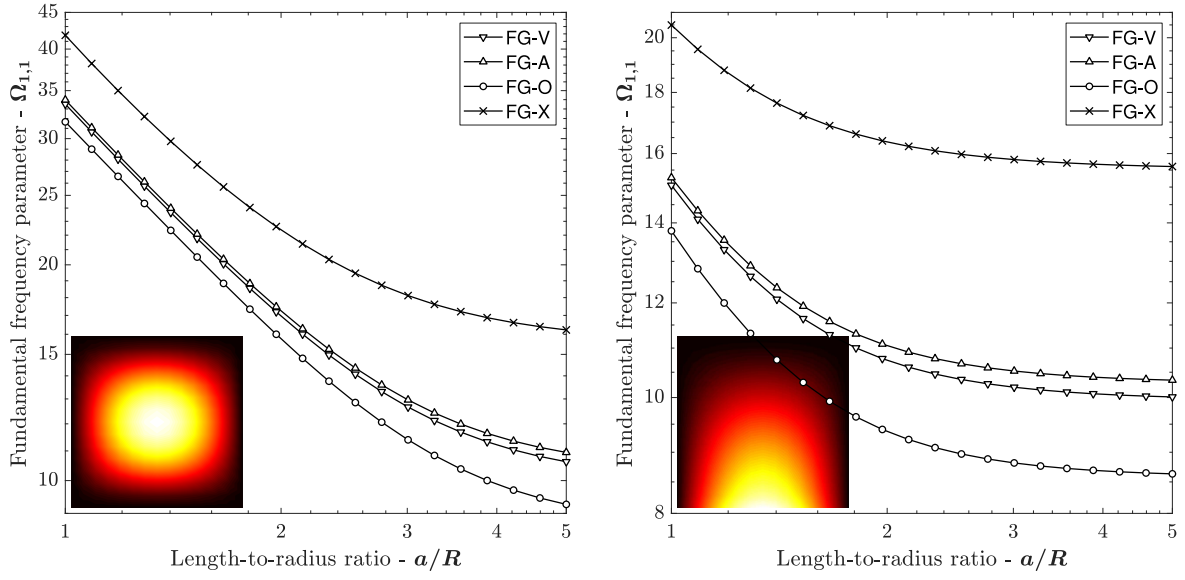

Figure 6: Fundamental frequency parameter vs length-to-radius ratio for a FG shell with $R/h = 10$, $\varphi = \pi/4$ and boundary conditions (radial displacement contour of the mode shape is reported at the outer surface): (a) CSCS; (b) FSCS.

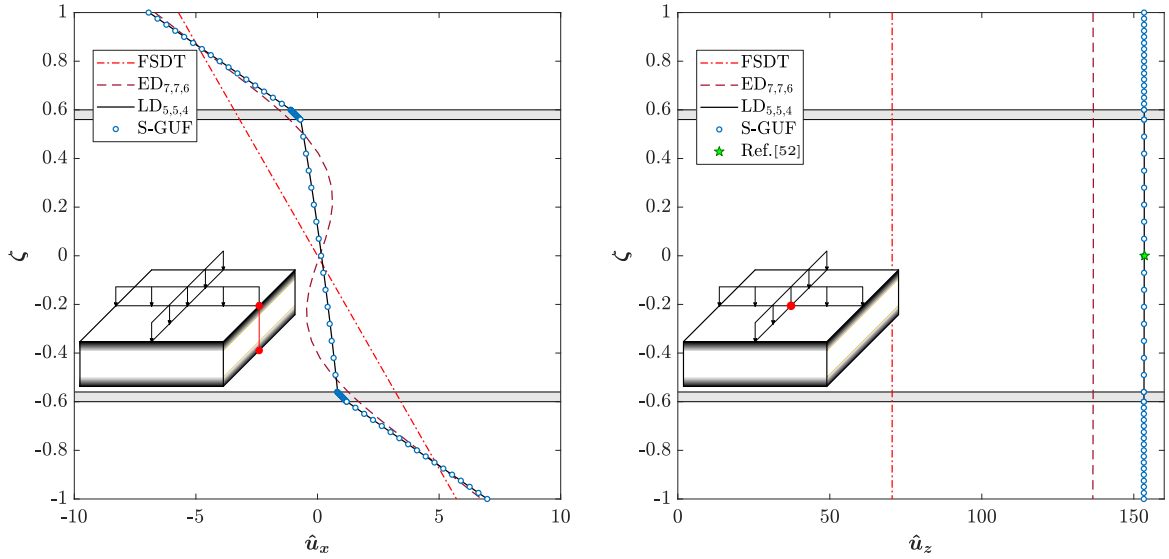

Figure 7: Through-the-thickness displacements in 5-layer sandwich square plate with $a = 1$ m and $a/h = 20$ subjected to uniform pressure load, using different kinematic theories and S-GUF ($\text{LD}_{1,1,0}$ / $\text{ED}_{3,3,2}$ / $\text{LD}_{1,1,0}$): (a) $\hat{u}_x$ at $x = 0$, $y = b/2$; (b) $\hat{u}_z$ at $x = a/2$, $y = b/2$.

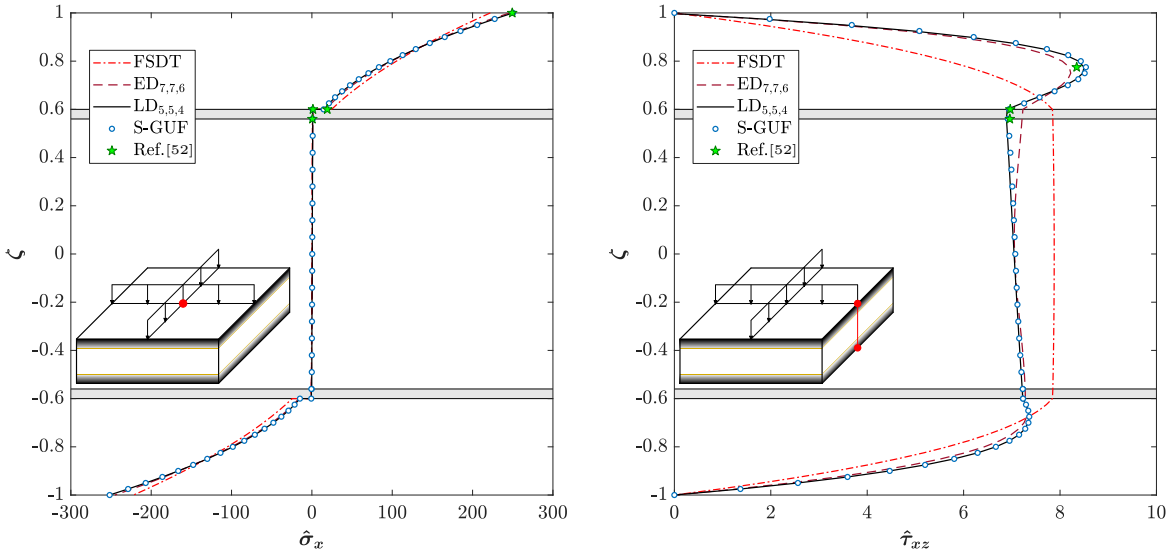

Figure 8: Through-the-thickness stresses in a 5-layer sandwich square plate with $a = 1$ m and $a/h = 20$ subjected to uniform pressure load, using different kinematic theories and S-GUF ($\text{LD}_{1,1,0}$ / $\text{ED}_{3,3,2}$ / $\text{LD}_{1,1,0}$): (a) $\hat{\sigma}_x$ at $x = a/2$, $y = b/2$; (b) $\hat{\tau}_{xz}$ at $x = 0$, $y = b/2$.

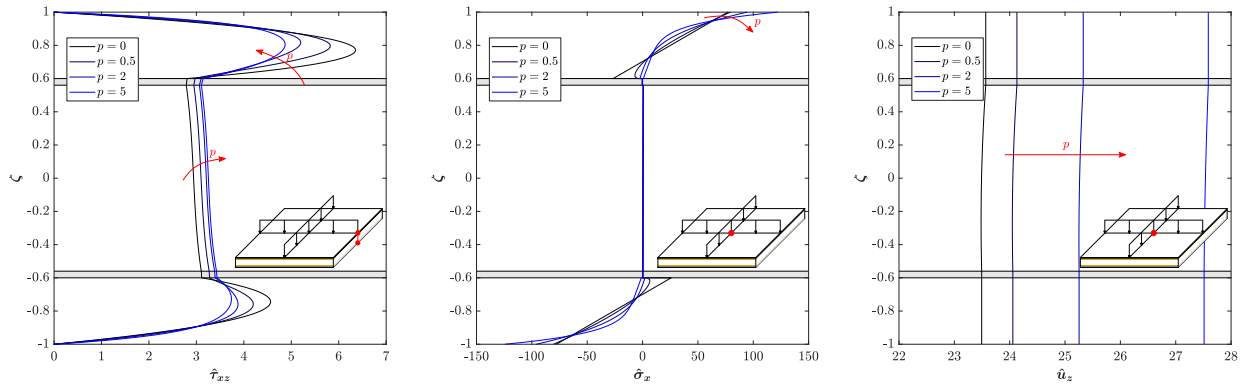

(a) (b) (c)

Figure 9: Effect of the inhomogeneity parameter for square plate with $a/h = 10$, $h_1/h = 0.2$. Face-sheets from fully ceramic to functionally graded metallic-to-ceramic with exponent $p \in (0, 5]$: (a) $\hat{\tau}_{xz}$ at $x = 0$, $y = b/2$; (b) $\hat{\sigma}_x$ at $x = a/2$, $y = b/2$; (c) $\hat{u_z}$ at $x = a/2$, $y = b/2$.

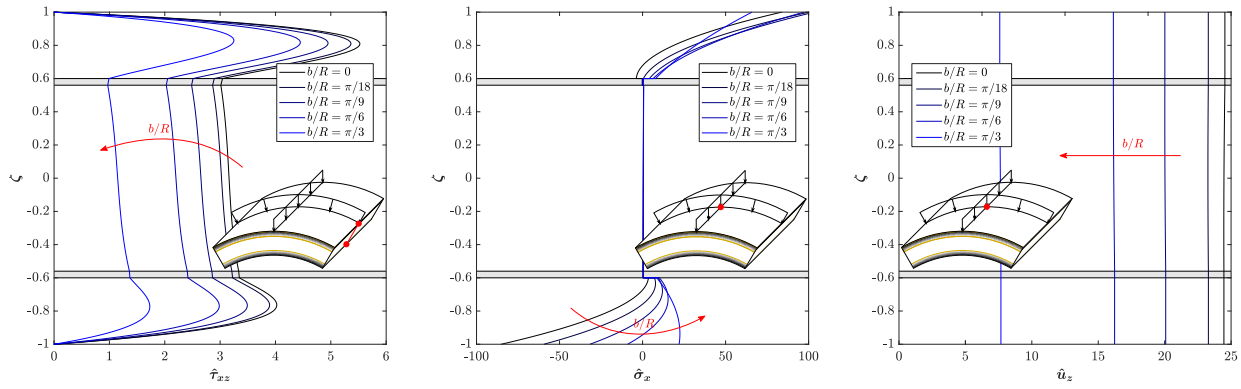

(a) (b) (c)

Figure 10: Effect of shallowness ration for shell with equal planar dimensions, $a/h = 10$, $h_1/h = 0.2$, $p = 1$. Width-to-radius ratio from zero (flat plate) to $\pi/3$ (deep shell): (a) $\hat{\tau}_{xz}$ at $x = 0$, $y = b/2$; (b) $\hat{\sigma}_x$ at $x = a/2$, $y = b/2$; (c) $\hat{u_z}$ at $x = a/2$, $y = b/2$.

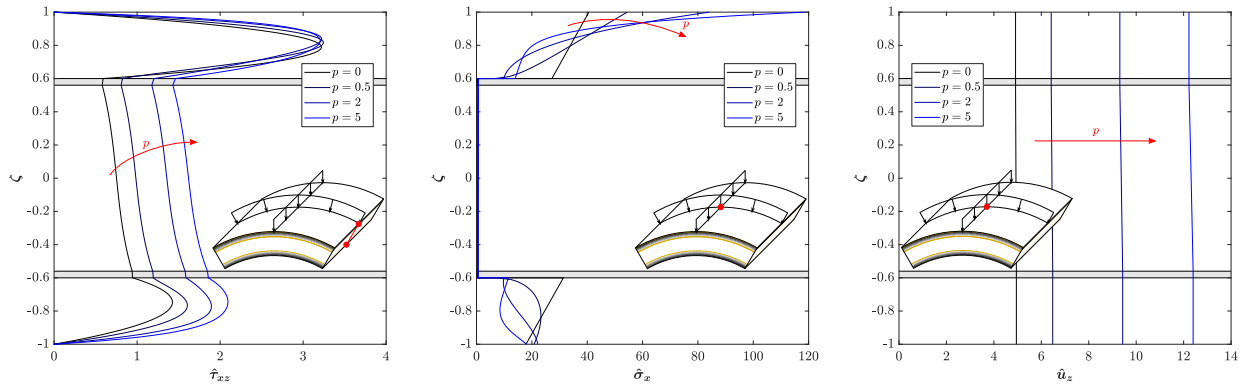

(a) (b) (c)

Figure 11: Effect of inhomogeneity parameter for shell with equal planar dimensions, $a/h = 10$, $h_1/h = 0.2$, $b/R = \pi/3$. Face-sheets from fully ceramic to functionally graded metallic-to-ceramic with exponent $p \in (0, 5]$: (a) $\hat{\tau}_{xz}$ at $x = 0$, $y = b/2$; (b) $\hat{\sigma}_x$ at $x = a/2$, $y = b/2$; (c) $\hat{u_z}$ at $x = a/2$, $y = b/2$.

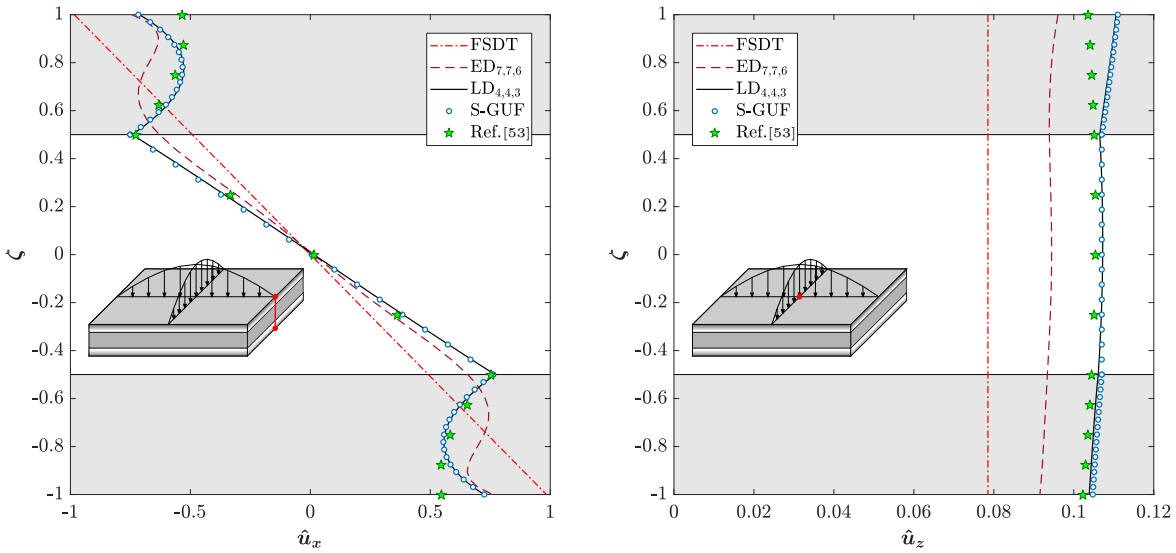

Figure 12: Through-the-thickness displacements in thick 3-layer sandwich square plate with FG-CNTRC skins and $a/h = 5$ subjected to bi-sinusoidal pressure load using different kinematic theories and S-GUF stands for ($ED_{3,3,2}$ / FSDT / $ED_{3,3,2}$): (a) non-dimensional in-plane displacement $\hat{u}_x$ evaluated at $x = 0$, $y = b/2$; (b) non-dimensional transverse displacement $\hat{u}_z$ evaluated at $x = a/2$, $y = b/2$.

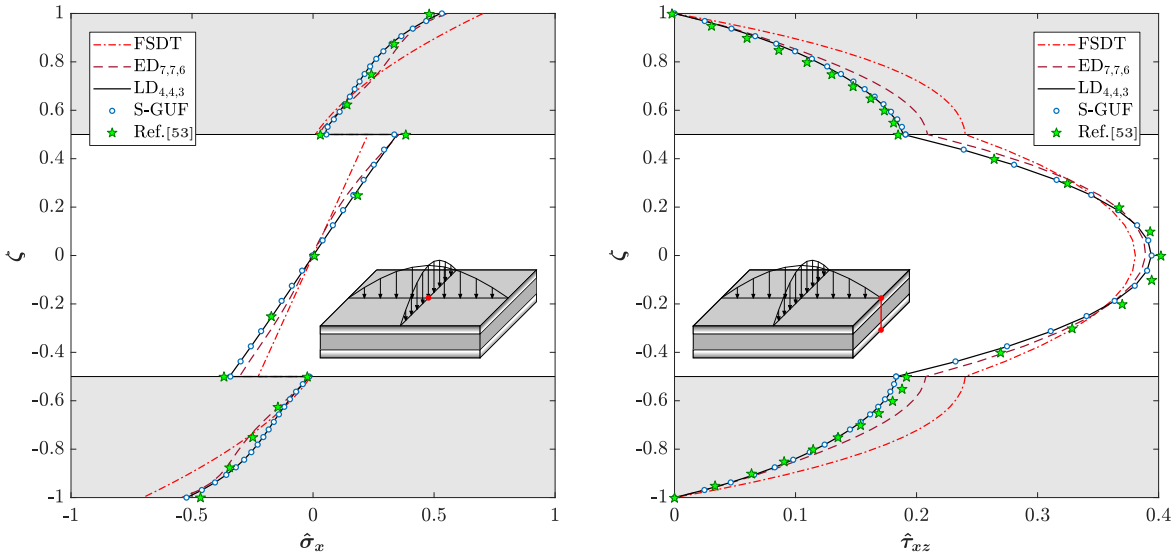

Figure 13: Through-the-thickness stresses in thick 3-layer sandwich square plate with FG-CNTRC skins and $a/h = 5$ subjected to bi-sinusoidal pressure load using different kinematic theories and S-GUF ($ED_{3,3,2}$ / FSDT / $ED_{3,3,2}$): (a) $\hat{\sigma}_x$ at $x = a/2$, $y = b/2$; (b) $\hat{\tau}_{xz}$ at $x = 0$, $y = b/2$.

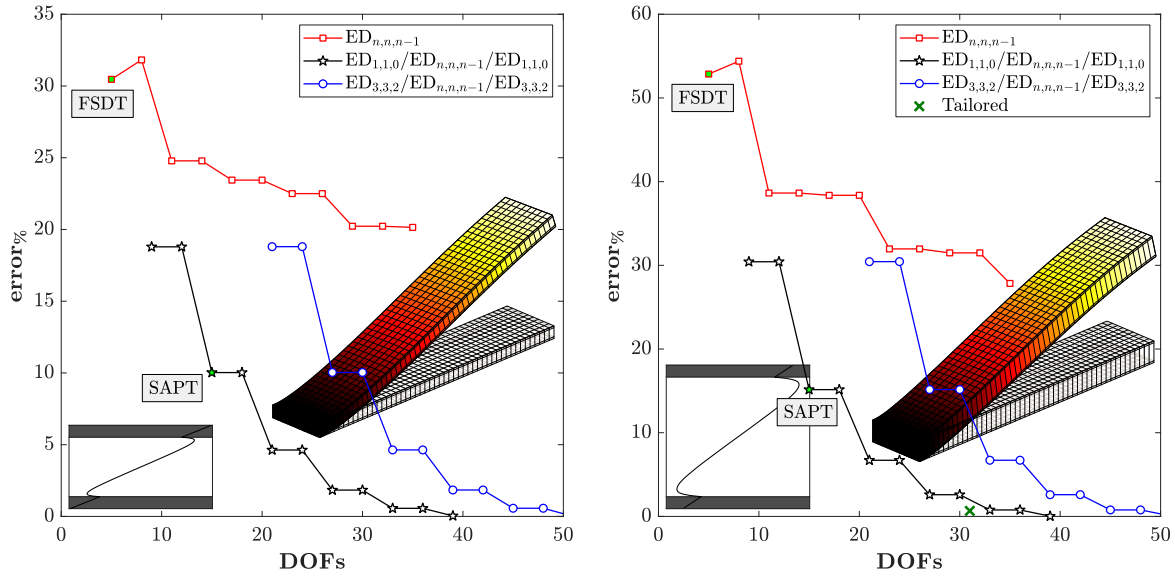

Figure 14: Relative error in computing the fundamental frequency with respect to quasi-3D results, FG-O core: (a) $h_c/h_s = 5$, Mode 1 @726.51 rad/s; (b) $h_c/h_s = 10$, Mode 1 @1077.5 rad/s, the "tailored" model is $\text{ED}_{1,1,0}$ / $\text{ED}_{4,4,3}$ / $\text{ED}_{1,1,0}$ / $\text{ED}_{4,4,3}$ / $\text{ED}_{1,1,0}$.

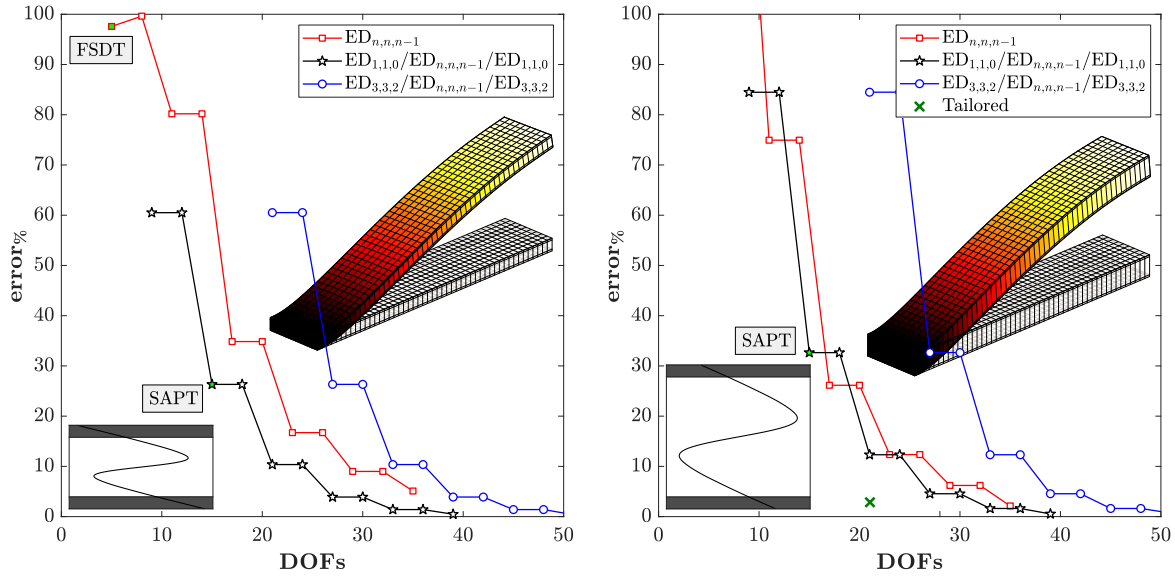

Figure 15: Relative error in computing the fundamental frequency with respect to quasi-3D results, FG-X core: (a) $h_c/h_s = 5$, Mode 1 @485.80 rad/s; (b) $h_c/h_s = 10$, Mode 1 @648.32 rad/s, the "tailored" model is $ED_{1,1,0}$ / $ED_{5,5,4}$ / $ED_{1,1,0}$.

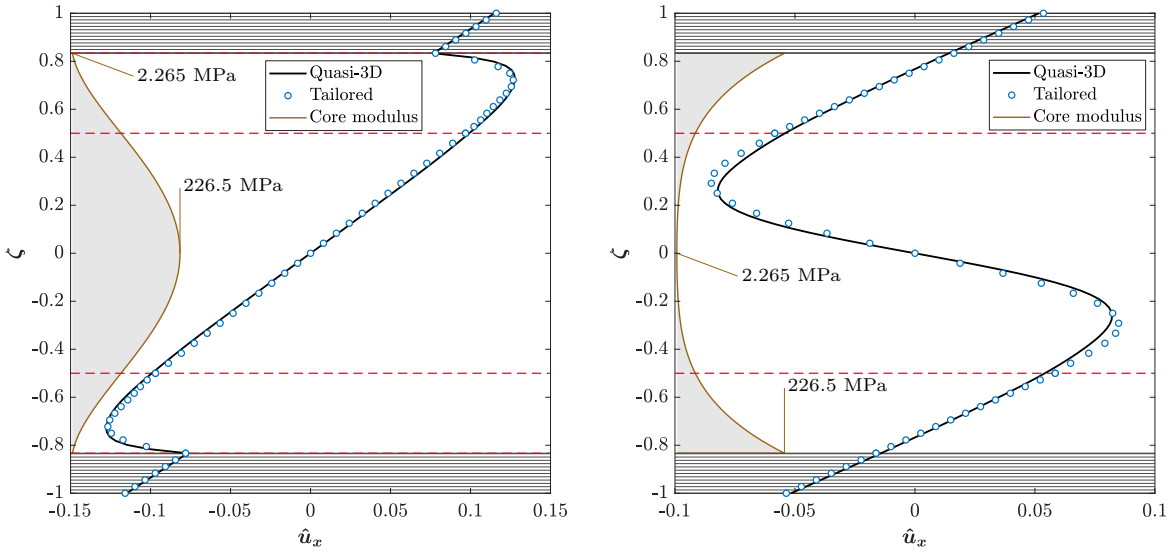

Figure 16: Modal displacement computed splitting the core in three mathematical layers: (a) FG-O core, $ED_{1,1,0}$ / $ED_{4,4,3}$ / $ED_{1,1,0}$ / $ED_{4,4,3}$ / $ED_{1,1,0}$; (b) FG-X core, $ED_{1,1,0}$ / $ED_{5,5,4}$ / $ED_{1,1,0}$.